SYNTHESIS OF DOPED AND UNDOPED ZNO NANOSTRUCTURES VIA CHEMICAL VAPOR DEPOSITION FOR APPLICATIONS IN DYE-SENSITIZED SOLAR CELLS

_____

A Thesis

Presented to

The Faculty of the Department of Chemistry

Sam Houston State University

_____

In Partial Fulfillment

of the Requirements for the Degree of

Master of Science

_____

by

Parker O. Blount

May 2022

SYNTHESIS OF DOPED AND UNDOPED ZNO NANOSTRUCTURES VIA CHEMICAL VAPOR DEPOSITION FOR APPLICATIONS IN DYE-SENSITIZED SOLAR CELLS

by

Parker O. Blount

_____

APPROVED:

Tarek M. Trad, PhD
Committee Director

David E. Thompson, PhD
Committee Member

Darren L. Williams, PhD
Committee Member

John B. Pascarella, PhD
Dean, College of Science and Engineering Technology

ABSTRACT

Blount, Parker O., *Synthesis of doped and undoped ZnO nanostructures via chemical vapor deposition for applications in dye-sensitized solar cells*. Master of Science (Chemistry), May 2022, Sam Houston State University, Huntsville, Texas

Nanostructure synthesis of wide band gap transparent conductive oxides (TCO) has been garnering significant interest in optoelectronics. They have different characteristics than their bulk counterparts, particularly larger surface area to volume ratio, leading to increased performance. Zinc oxide is a wide band gap TCO that is non-toxic, cheap, and has impressive electron mobility. The effects of Sb doping and Cu doping on ZnO nanowires grown by a novel chemical vapor deposition method that uses an inner reaction tube to promote uniformity and scalability were investigated. Undoped ZnO nanowires were first synthesized and grown in the wurtzite crystal phase. They had a diameter of ~130 nm and expressed a lower bandgap than bulk ZnO. The undoped nanowires expressed oxygen-vacancy (V_O) defects as well as evidence of additional defects including zinc-vacancies (V_{Zn}) that may be responsible for p-type conductivity. The Sb-doped ZnO nanostructures were much larger in diameter being 289 nm and 306 nm for the two separate oxidation states of the antimony precursor. X-ray diffraction (XRD) showed decreased crystallinity with slight peak shifts, which could be a direct result of Sb doping. Photoluminescence data showed a decrease in the bandgap and electron-hole (e^--h^+) lifetime. Similar defects were expressed in Sb(III)-doped ZnO as the undoped nanowires, but Sb(V)-doped ZnO showed much less evidence of V_O. Cu-doped ZnO had a decrease in diameter to 80 nm. XRD showed no shifts in the Bragg angles, while energy dispersive X-ray spectroscopy (EDS) showed 1.11% - 1.71% incorporation of Cu into the ZnO crystal lattice. A decrease in the bandgap and an increase in e^--h^+ lifetime were determined from photoluminescence data. There is also evidence of a significant decrease in V_O defects. The

undoped ZnO nanowires were used as a working electrode for a dye-sensitized solar cell. Initial experiments did not show any significant power conversion efficiencies for the developed cells, which could be due to several factors. However, continuing efforts are being made to develop “functioning” dye-sensitized solar cells using metal oxide nanostructured electrodes prepared in this project.

KEYWORDS: Nanostructures, Zinc oxide, Chemical vapor deposition, Dye-sensitized solar cells, Photovoltaics, Semiconductors

ACKNOWLEDGEMENTS

I believe it goes without saying that I would not have been able to complete this work without my advisor, Dr. Tarek Trad. His constant guidance and ability to push me through the toughest times were invaluable, and without him, I would not be the chemist I am today. He has been a great mentor and great friend. I am also extremely grateful to my other two committee members Dr. Darren Williams and Dr. David Thompson. Both have been great mentors throughout my entire academic career and have been invaluable to my growth and development as a chemist. I always knew talking to either one of these gentlemen, at any given time, was going to lead to a valuable lesson; chemistry-related or not.

I would like to give great thanks to my friends and family that have helped me through this journey. My fiancé, mom, dad, brother, and grandmother were all huge supporters, and I couldn't have done this without them. I also want to give great thanks to all the Trad research members past and present with a special thank you to Morgan Johnson. Over the past several years, their collegiality and support will be treasured for years to come.

I would also like to give thanks to Dr. Donovan Haines, Rachell Haines, and Dr. Dustin Gross for their assistance and advice throughout my academic career at SHSU. I am grateful to them for being there whenever I needed them.

TABLE OF CONTENTS

Page

LIST OF FIGURES

CHAPTER I

Introduction

Motivation

Global population growth, exponential industrialization, and the dramatic increase in energy demand are among the main reasons for the continued increase in carbon emissions. The challenge of carbon emission control could be met with renewable energy solutions and better strategies to realize them economically. Solar energy is easily harnessed with the use of photovoltaic cells that utilize the unique properties of semiconducting materials.

Semiconductors have several characteristics that make them an attractive material to study. They have a bandgap that is larger than conductors and lower than insulators. This correlates to them having an electronic conductivity that is lower than conductors but higher than insulators. Their resistivity is variable and dependent on temperature. Semiconductors are optically transparent in the near IR region and typically absorb light in the visible region. They are lightweight and have the ability to fit into microprocessors alongside several other devices and applications. Semiconductors form electron-hole (e^--h^+) pairs when absorbing photons. The speed at which these carriers can move in an electric field is known as carrier mobility, which is an important property for determining the suitability of semiconductors in applications for many electronic devices. The thermal conductivity of semiconductors is determined by the number of free electrons and holes in the material. The importance of this is apparent in the fabrication and application of the

semiconductor, as thermal conductivity is an important parameter for determining the maximum power at which a semiconductor can operate.

Zinc Oxide Properties and Applications

There are several modern devices and applications that utilize semiconductors but discovering ways to improve these devices could lead to exponential growth in technology. These improvements come in the form of increased performance, reduced cost, or smaller environmental impact. Zinc oxide (ZnO) is garnering more attention for these exact reasons. ZnO is a II-IV compound semiconductor that has a direct and wide bandgap of 3.37 eV, has a high electron mobility of 60 meV, is piezoelectric, fairly cheap[1], and is non-toxic. ZnO is found in three crystal phases: zinc blende, wurtzite, and rock salt (Figure 1).

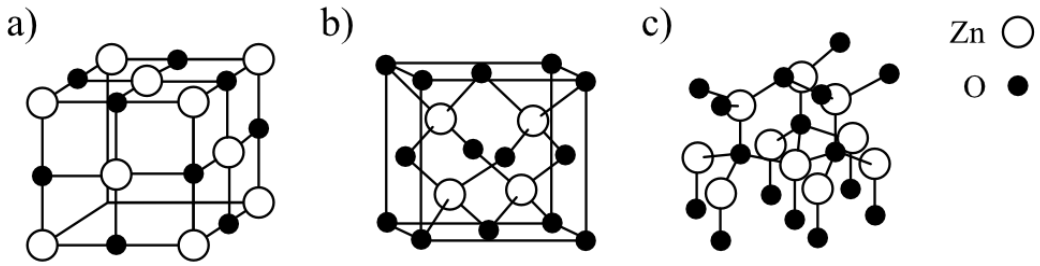

Figure 1. The crystal phases of ZnO: rock salt (a), zinc blende (b), and wurtzite (c).

Zinc blende and wurtzite are both tetrahedral in geometry that is equivalent to sp3 hybridization in covalent bonding, but ZnO has significant ionic character, which means less orbital overlap and an increase in its bandgap. Zinc blende is a part of the space group F-43m. This cubic crystal can only be synthesized in the lab on substrates that already contain a cubic lattice structure, such as metal-organic framework-5 or MOF-5.[2] This is

due to zinc blende being metastable because it has more covalent bonding than that of its structural counterparts.[3] The wurtzite crystal phase is more stable in experimental conditions and does not require a template, thus making it the most common crystal phase in ZnO nanoparticle synthesis.[4] ZnO's wurtzite structure can be described as non-centrosymmetric with polar surfaces and is in the $P6_3mc$ space group. It is composed of two hexagonal close-packed (hcp) sublattices of Zn and O with a c/a ratio of $(8/3)^{1/2}$ and oxygen anions fill half of the tetrahedral sites. Rock salt has an extreme ionicity similar to the other well-known rock salt, halite (NaCl). ZnO's crystal phase of rock salt is only found in extremely high temperatures and pressures and does not see much use in nanomaterial studies.

ZnO's attractive qualities have already placed it in optoelectronic applications like gas sensors[5], UV detectors[6], and photovoltaic cells.[7] Most of these applications use the nanostructures of ZnO rather than its bulk counterpart. Nanoscale applications of ZnO, along with most semiconductors, are what allow it to be used in such small devices with exceptional performance. ZnO nanoparticles can come in a large variety, which is dependent on the synthesis method. The type of method can heavily influence the nanoparticle's size, morphology, composition, and crystal phase.

ZnO Nanoparticle Synthesis

There are several avenues of ZnO nanoparticle synthesis which can be classified as either green, chemical, or physical methods. Green methods make use of biological reagents to synthesize ZnO nanoparticles.[8] Most commonly fruits or leaves are ground up and washed with water. The solution is then heated to begin extracting all the various

compounds within the fruit. The compounds that are found in the biological extractors include alkaloids, terpenes, polyphenols, flavonoids, and many others. These compounds can act as either reducing, capping, or stabilizing agents that are the main contributors to synthesizing ZnO nanoparticles from a solution containing a Zn salt.[9]

Chemical avenues of ZnO nanoparticle synthesis use a Zn salt along with various solvents, reagents, and bases. Commonly used chemical methods include hydrothermal, sol-gel, and co-precipitation. Hydrothermal synthesis is straightforward as you start with a Zn salt and a precipitant providing OH^- to form a precursor. Typically, urea or some other base is used to adjust the pH of the solution. The precursor is then transformed into ZnO via heat treatment.[10] Sol-gel and co-precipitation routes are similar in methodology.[11,12] These methods have the advantage of being able to produce ZnO nanoparticles at relatively low temperatures, which is vital for upscaling to industrial levels of production. However, the disadvantages become apparent in the quality of the crystal that is produced and the amount of organic solvent wasted in the process.

Physical methods share a common advantage of very limited use of organic solvents to produce high-quality ZnO nanoparticles. Common physical synthesis methods include pulse laser deposition[13], molecular beam epitaxy[14], and chemical vapor deposition (CVD)[15]. These methods suffer from several disadvantages which include high equipment and usage cost, high operating temperatures, and low pressures. Of the physical methods, CVD techniques are typically the most cost-effective.

Chemical vapor deposition is a vapor phase transport process capable of producing high-quality crystalline structures on fixed substrates. This process is tunable and can be variably configured by changing reaction conditions such as temperature, pressure, carrier

gas flow, and nature of precursor. This process typically involves a volatile precursor, a carrier gas, a reactive gas, and a substrate. The precursor is vaporized where it can interact with the reactive gases in the system. Gaseous reagents travel to a lower temperature area where a substrate with a catalytic surface like gold or a thin film of the desired material promotes nanostructure growth. In the case of ZnO applications, the starting material is typically either Zn metal or ZnO which are extremely non-volatile. Zn metal sublimes at 343 °C at atmospheric pressure and ZnO has a vaporization temperature of 1975 °C. Since these precursors need to be in the gaseous phase to react several techniques are used to initiate their high-energy reactions. These techniques include the addition of heat via a furnace[16], plasma-assistance[17], laser-assistance[18], or a combination of the three. To reduce the amount of heat or energy that is needed to vaporize these precursors, a substance that can thermally reduce the precursor, like carbon, can be added to lower the overall decomposition temperature of the precursor. Reaction time, reaction temperature, pressure, gas flow, and deposition temperature will affect several properties of the synthesized nanoparticles. The ability to easily manipulate these variables is another advantage of the CVD method and physical synthesis methods in general.

Solar Cell Applications of Metal Oxides

Originally, photovoltaic cells were made of two amorphous silicon layers, one being bare silicon, an intrinsic n-type semiconductor, and the other doped silicon with an element such as boron that produces p-type semiconducting properties.[19] These cells came into existence along with the discovery of the photovoltaic effect. The difference in bandgap and charge of the two layers allow for the separation and flow of electrons and

their holes when a photon interacts with the junction. These cells are still being studied today but use various semiconductors as well as Si nanostructures to increase performance.[20]

Recently, the literature is taking a new direction by looking at new types of solar cells: perovskite and dye-sensitized. These photovoltaic cells are similar in function but differ in design. The design of these cells starts with a light-harvesting agent, whether it be a dye or solid-state crystal, injecting an electron or a hole into a wide-band semiconductor and allowing the flow of charge carriers (e^- and h^+). Perovskite cells use a crystal as a light harvester, most commonly methyl ammonium lead iodide [$(CH_3NH_3)PbI_3$], which was the first stable perovskite solar cell to achieve an impressive efficiency of 9.7%.[21] Currently, high performing perovskite solar cells have reached efficiencies exceeding 25%.[22]

The photovoltaic conversion efficiency (PCE) can be described as the amount of incident sunlight converted to usable electricity. PCE (η) is calculated by dividing the power out of the cell by the power put into the cell (Equation 1).

$$\eta = \frac{P_{out}}{P_{in}} \times 100\% \quad (1)$$

Although PCE is typically the main determinant of how well a cell is performing when compared to another, the fill factor describes the maximum power of the solar cell (Equation 2). Fill factor (FF) is directly proportional to the maximum power and inversely proportional to short-circuit current (I_{SC}) and open-circuit voltage (V_{OC}). The ideal solar cell would have both a high efficiency and fill factor.

$$FF = \frac{P_{max}}{I_{SC}V_{OC}} \quad (2)$$

Perovskite solar cells primarily use wide-bandgap metal oxides like TiO_2 as their electron transport layer (ETL)/hole transport layer (HTL), due to their success in dye-sensitized solar cells prior.[23,24] The difference between ETL and HTL is based on the type of semiconductor being used, which is either n-type (ETL) or p-type (HTL). Several metal oxides are being investigated as an ETL or HTL including Cu_2O/CuO[25], SnO_2[26], and ZnO[27]. These metal oxides are not limited to just being used in perovskite cells, but in dye-sensitized and heterojunction cells as well where they perform an identical role.

Cuprous oxide is an inherent p-type semiconductor with a bandgap of 2.17 eV. Cu_2O is very popular in all-oxide photovoltaic cells.[28] Which are multilayer heterojunction cells that work by only using metal oxide semiconductors as components in their design. All-oxide cells are non-toxic, chemically stable, and use metal oxides that are high in abundance. The reason for its popularity in all-oxide PV cells is the need to optimize the Cu_2O band gap. The optimization of the bandgap can be achieved by the design of the heterojunction cells. This is because a heterojunction cell has multiple metal oxides with different bandgaps and different semiconducting properties (n-type or p-type) that influence the bandgap. In single-junction devices, which are reliant on the single metal oxide that is available, it is much more difficult, but not impossible, to change the bandgap drastically. With its original bandgap of 2.17 eV, the theoretical efficiency limit is ~23%, but when optimized and lowered to a bandgap of 1.34 eV the theoretical limit rises to 32.9%.[29] This theoretical efficiency is also known as the "detailed balance limit." Which looks at the complete conversion of e^--h^+ in a solar cell. To explain further, photovoltaic cells act as a blackbody radiator that emits electromagnetic waves, which decreases the efficiency of the cell. The detailed balance limit ignores this and strictly looks at band-to-

band recombination of the electron and the holes. Of course, this can never truly be achieved but it does give researchers an idea of what materials are worth looking at in the field of photovoltaics.

Tin oxide is being used in many different photovoltaic cells like perovskite, heterojunctions, and dye-sensitized due to its very familiar and attractive properties. Much like TiO_2, SnO_2 is a wide bandgap (3.6 eV) n-type semiconductor with high electron mobility and low UV degradation. Michael Grätzel, known for his pioneering work in dye-sensitized solar cells, and coworkers fabricated a high-performance perovskite cell using tin oxide (SnO_2).[26] It has also seen use in organic bulk heterojunction solar cells due to its inertness and high transmittance.[30] Recent literature shows a PCE of greater than ~20% when used in perovskite cells.[31] With it being generally cheaper than TiO_2, SnO_2 has a high potential to surpass TiO_2 in PV cell applications.

ZnO in Dye-Sensitized Solar Cells

In 1991, Grätzel and O'Regan pioneered metal oxide-based dye-sensitized solar cells.[23] Their TiO_2 solar cell achieved a light to electric conversion efficiency of 7.1-7.9% in simulated sunlight (Figure 2).

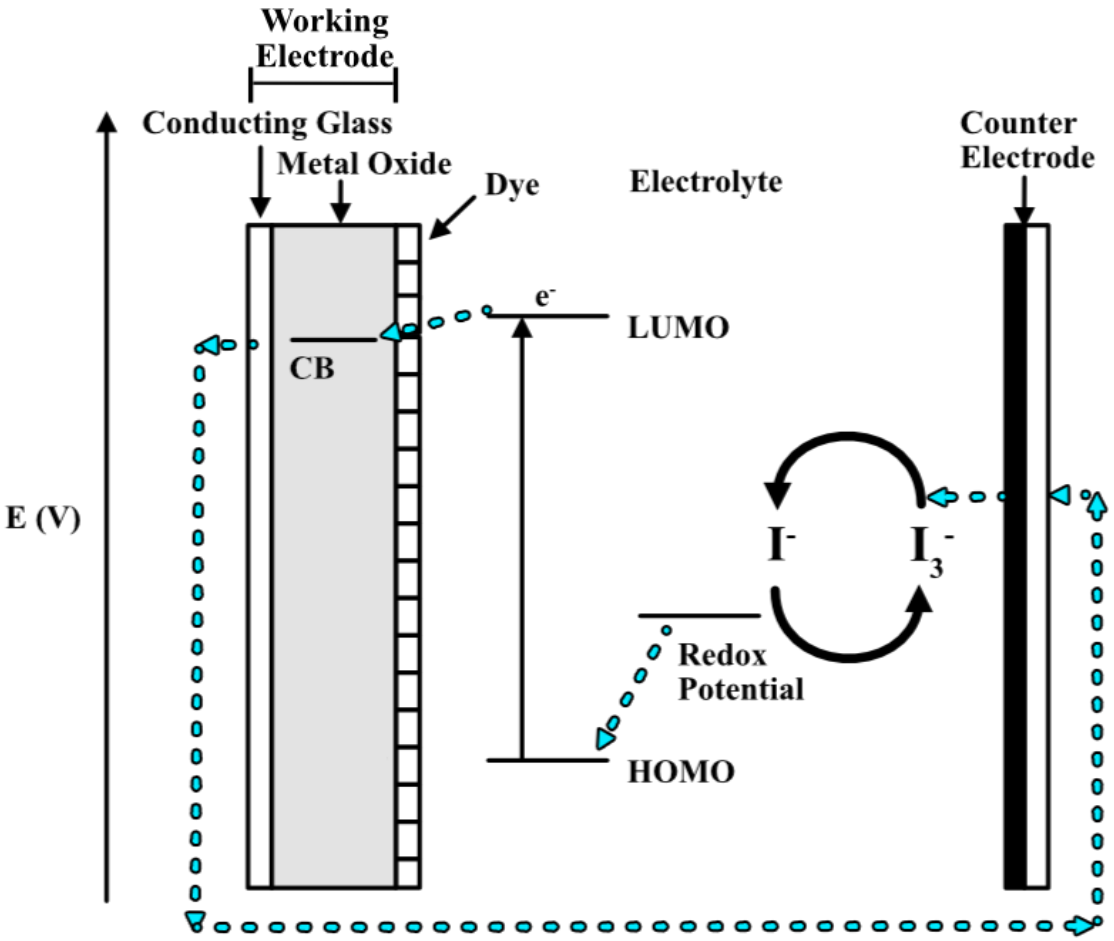

Figure 2. The original design of a Grätzel type dye-sensitized solar cell.

Dye-sensitized solar cells consist of 5 major components: a working electrode, a metal oxide, a photoactive dye, an electrolyte, and a counter electrode. Both electrodes typically consist of transparent conductive glass with either the metal oxide grown on it (working electrode) or an electron facilitator like platinum (counter electrode). The electrolyte is used to oxidize or reduce the dye, depending on whether the cell is using an n-type or p-type semiconductor. The dye that is used in these cells is photoactive and preferably absorbs light from the UV to near IR region.

Dye-sensitized solar cells can be described simply as a diode that absorbs a photon from the sun using a dye and produces a current. The photon excites an electron from the HOMO to the LUMO of the dye, leaving behind a hole in its place. The electron is then injected into the conduction band of the metal oxide. The energy of the conduction band must be lower than that of the LUMO of the dye. Electrons will not flow otherwise. The electron is then passed to an external circuit where it will eventually contact the backside of the counter electrode. The electrolyte solution is used to reduce the dye and regenerate it back to the ground state. This then allows for the flow of electrons from the counter electrode to the dye and reduces it as well. It is also possible to follow the movement of the holes. Instead of the electrolyte reducing the dye and regenerating it, one could think about the hole oxidizing the electrolyte. This idea of the movement of holes is more important when talking about p-type doping and will be discussed in chapters III, IV, and V.

The highest recorded efficiency for a ZnO-based dye-sensitized solar cell is 8.22% in 2018.[32] This is a very large increase compared to where it started back in 1994 at 0.4%.[33] This is still behind the highest efficiency achieved by a TiO2-based cell at 13%, even though ZnO has greater electron mobility than TiO_2.[34] The limitation of ZnO-based solar cells can be attributed to a few things. First, is the formation of Zn^{2+}/dye aggregates that form from the adsorption of the acidic dye onto the ZnO electrode which not only promotes recombination of e^--h^+ pairs but is also destructive to the ZnO crystal surface.[35,36] Another issue is the interaction between the electrolyte and ZnO that also causes e^--h^+ recombination and consequently a reduction in the overall efficiency.[32] Slow injection of electrons from ZnO is another issue that is limiting ZnO-DSSCs performance. This slow

electron injection stems from a decreased amount of density of states in the conduction band of ZnO compared to that of TiO_2.[37] One could assume that if the number of electrons allowed in the conduction band of ZnO is less than TiO_2 then n-type ZnO based DSSCs performance will never surpass that of TiO_2. Because they do not rely on a high density of states in the conduction band, p-type ZnO may be the better form to compete with the performance of TiO_2 based DSSCs.

Objectives

The objective of this investigation is to synthesize undoped and Cu/Sb-doped ZnO nanostructures using a novel CVD method that focuses on scalability and uniformity while maintaining a high-quality crystal structure. The primary goal of these nanostructures is to be used as a working electrode in dye-sensitized solar cells. Optimization of the reaction time, temperature, and gas flow was investigated to determine the tunability of the method. The crystal morphology and composition were characterized using scanning electron microscopy (SEM) and energy-dispersive X-ray spectroscopy (EDS). The crystal phase and structural information of the nanowires were investigated using X-ray diffraction (XRD). Crystal quality and photoelectronic effects were looked at using room temperature photoluminescence (RT-PL).

CHAPTER II

Synthesis of Undoped Zno Nanocolumns via a Novel Chemical Vapor Deposition Method

Introduction

Undoped ZnO exhibits an inherent n-type semiconducting nature. The reason for this can be seen in its crystal structure. Typically, a large amount of oxygen vacancies is observed as surface-level defects in ZnO. An oxygen vacancy is a defect in the crystal structure where an O atom that should be bonded to 1 or more Zn atoms is not present. These are deep-level electron donors, which increase the electron richness of ZnO thus making it an n-type semiconductor. Another possibility for this behavior is the accidental doping of hydrogen in the crystal lattice. If a ZnO nanostructure synthesis reaction is exposed to hydrogen, there is a possibility that H will fill an interstitial site and act as a donor within the structure.[38] The donor properties of H stem from donating a single electron to the system and appearing in the H^+ oxidation state while in the structure.

Synthesis of ZnO nanoparticles is a feat that is easily achievable by a variety of methods. Chemical methods such as hydrothermal and sol-gel can produce ZnO nanoparticles reliably, at relatively low temperatures, and at a low cost. The main disadvantages are the lack of crystal quality and the large amount of waste produced from solvents and other reagents. Physical methods are an alternative to their chemical counterparts that produce much less waste at the cost of having to perform the synthesis at extreme temperatures and pressures, as well as, having very costly instrumentation. Chemical vapor deposition is a method that has a lower upfront cost than other physical

techniques such as pulse laser deposition and molecular beam epitaxy, while still being able to produce the high-quality crystals that chemical methods struggle to achieve.

In this chapter, ZnO was synthesized using a novel chemical vapor deposition method that utilizes an inner reaction tube (Figure 3).

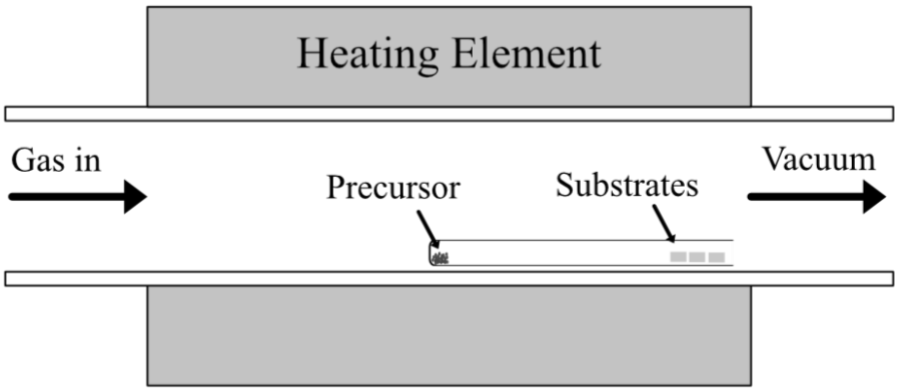

Figure 3. Schematic of the inner reaction tube CVD method.

The precursor is placed at the bottom of the inner reaction tube and the 1 cm x 1 cm silicon substrates are placed at the mouth. The reaction tube is then placed into the horizontal tube furnace aligning the ZnO precursor with the heating element and the substrates at the desired reaction temperature. It is important to note that the opened end of the reaction tube is facing the direction of the vacuum. This will cause an Eddy flow that allows the carrier gas to enter the reaction tube and interact with the gases produced from the precursor. The tube is sealed off and a vacuum is placed onto the system. Argon gas is introduced into the system as a carrier gas. The purpose of the inner reaction tube is to increase Zn and O richness at the reaction site. The increased density of elemental products will promote high ZnO nanowire uniformity and scalability. The reaction of ZnO is described in equations 3, 4, and 5.

$$ZnO_{(s)} + C_{(s)} \rightarrow Zn_{(g)} + CO_{(g)} \quad (3)$$

$$2ZnO_{(s)} + C_{(s)} \rightarrow 2Zn_{(g)} + CO_{2(g)} \quad (4)$$

$$2Zn_{(g)} + O_{2(g)} \rightarrow 2ZnO_{(s)} \quad (5)$$

ZnO reduces at 950 °C when in the presence of carbon. Carbon reacts with the oxygen from the ZnO and forms either CO (Equation 3) or CO_2 (Equation 4). Any excess O reacts with Zn at the substrate that will have a catalytic layer present, such as gold or a ZnO seed layer (Equation 5). This particular method does not require the addition of a reaction gas. The oxygen from the precursor or any impurities from the carrier gas is enough to push the reaction forward and give the desired results. The ZnO nanowires were grown at different synthesis times, then characterized via XRD, SEM-EDS, and RT-photoluminescence.

Materials and Methods

ZnO nanoparticle synthesis

Three silicon substrates (Ted Pella, Inc – Si(100)) were cut into 1 cm x 1 cm pieces. These substrates were sonicated in an ethanol (Sigma-Aldrich – 200 proof) bath for 10 minutes. Followed by sonication in an acetone (VWR Chemicals – 99.5%) bath for 10 minutes before being dried under nitrogen gas. A ZnO seed layer was prepared by coating the surface of the substrates with a 5.5 mM solution of zinc acetate (Sigma-Aldrich – 98%) and allowing it to evaporate completely. Zinc acetate is deposited on the surface while the solvent is evaporated off. The substrates were then heat-treated in a 160 °C furnace for 45 minutes. A combustion reaction takes place during this step that involves zinc acetate and oxygen from the air forming ZnO, CO_2, and H_2O. This process was repeated once more

with the same zinc acetate solution and heat-treated for 60 minutes rather than 45. A 50 mg mixture consisting of a 1:1 mole ratio of ZnO (Goodfellow – 99.999%) to C (Aldrich - <20 µm, synthetic) was used as a precursor. The precursor was placed at the bottom of a quartz reaction tube (1.2 cm i.d. x 25 cm) that had a single opened end. The prepared silicon substrates were placed at the mouth of the quartz reaction tube, in contact with one another, with the seed layer exposed. A temperature profile was performed to identify the temperature range of the furnace (Figure 4). The quartz tube was then placed in the horizontal tube furnace (MTI Corporation – OTF-1200X) with the middle substrate being placed in an area that was measured to have a temperature of ~730 °C when the furnace is active, and the precursor placed in the middle of the heating element. The reaction takes place at 950 °C (with a ramp time of 10 °C/min) with reaction times ranging from 15 – 90 minutes. The system was placed under vacuum with a pressure of 2.55 Torr using an oil roughing high vacuum pump (MTI Corporation – PV-HVS2). Ar gas (Ultra-High Purity) is introduced into the system via a mass flow controller (MTI Corporation – GSL-3Z). at 80 sccm. Following the reaction, the system is shut down, and the substrates are annealed for 12 - 24 hours.

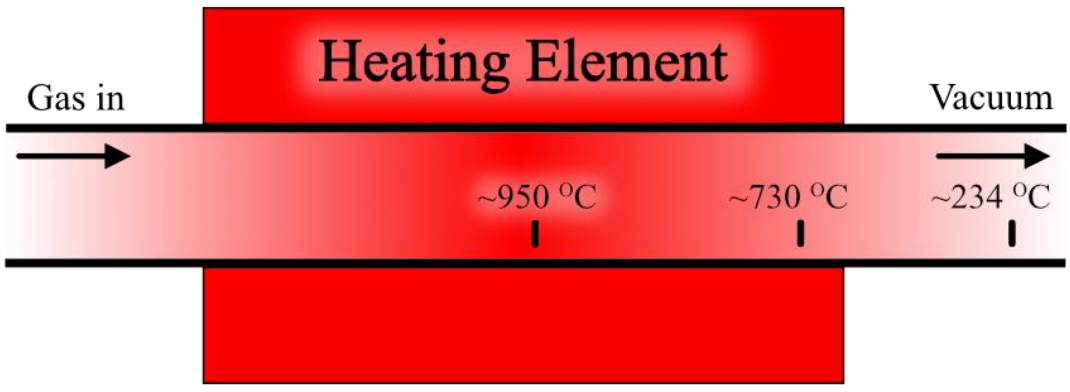

Figure 4. Temperature profile of the horizontal tube furnace.

Nanoparticle morphology, composition, and structural analysis

Nanoparticle size and shape were analyzed using scanning electron microscopy. Relative mass percentages of product composition were determined using energy-dispersive X-ray spectroscopy. Room temperature crystal phase and structural data were investigated using a Rigaku Miniflex 600 benchtop X-ray diffractometer. The 2θ values were observed from 20° to 65° with a current of 15 mA and a voltage of 40 kV. The crystal phase of the structure was matched and identified by the crystallography open database (COD). Room temperature photoluminescence was analyzed using a Hitachi F-4500 Fluorescence Spectrometer. The excitation wavelength was set to 325 nm, and the scan went from 350 nm to 600 nm at 700V. The slit width for the excitation beam was 10 nm and 5 nm for the emission beam.

Results and Discussion

X-ray diffraction analysis

Powder X-ray diffraction was used in nanowire/nanocolumn crystal phase investigations (Figure 5). Reflections at 31.7° (1 0 0), 34.35° (0 0 2), 36.2° (1 0 1), 47.45° (1 0 2), and 62.85° (1 0 3) were observed for the ZnO nanocolumns. These peaks were indicative of the wurtzite crystal phase of ZnO (COD # 1011258). High intensity (0 0 2) plane reflections could suggest the preferential epitaxial growth direction from the substrate and the column or rod-like morphology. The peak at 32.9° was identified to be silicon which is the substrate that was used for synthesis. XRD also gives information on the quality and purity of the crystal. No other peaks were identified that indicated any other crystal phase of ZnO or any other material, which is evidence of a high-quality crystal. Furthermore, the sharpness of the peaks is indicative of high crystallinity products.

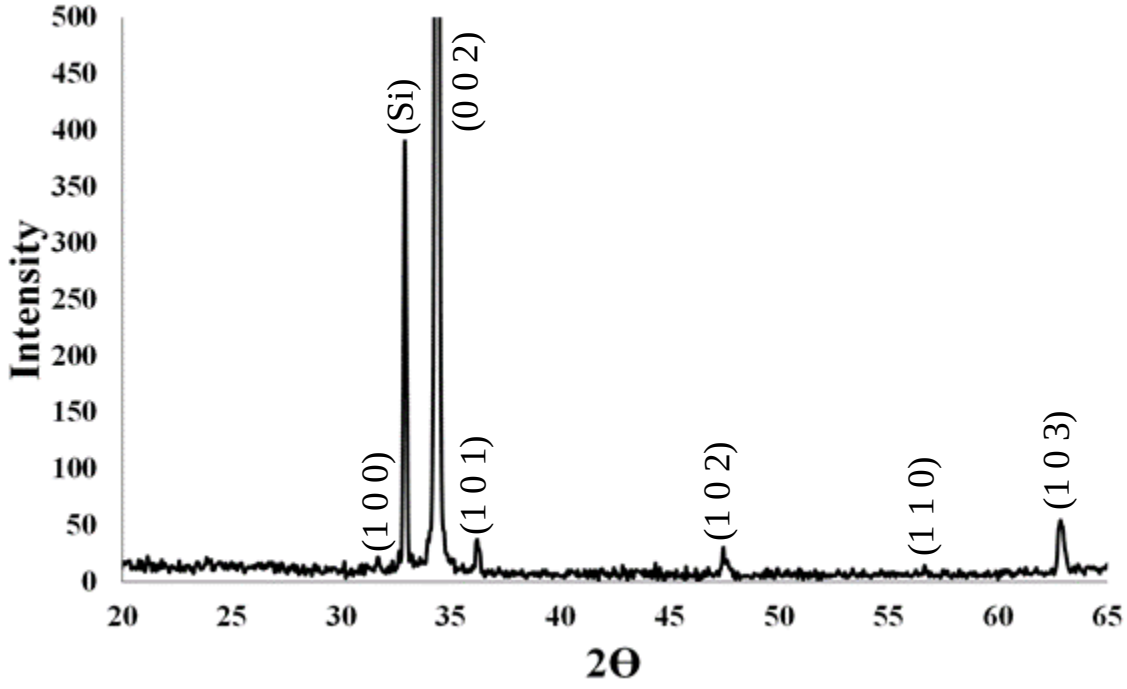

Figure 5. X-ray diffractogram of undoped ZnO nanocolumns grown on a silicon substrate.

Morphology and composition

The morphology of the ZnO nanostructures was investigated using scanning electron microscopy (Figure 6). SEM images show hexagonal columns semi-epitaxially grown from the substrate. Uniformity of the nanostructures was observed over the majority of the substrate surface, which can be seen in the inset of Figure 6. Concentrating elemental zinc gas in this inner-tube model could be advantageous in future scalability experiments. Elemental surface scans were performed using EDS to confirm the stoichiometry of ZnO. Atomic percentages were 44.60% for Zn and 55.40% for O. The atomic percentage is close to 50% for each element is further evidence of a ZnO product.

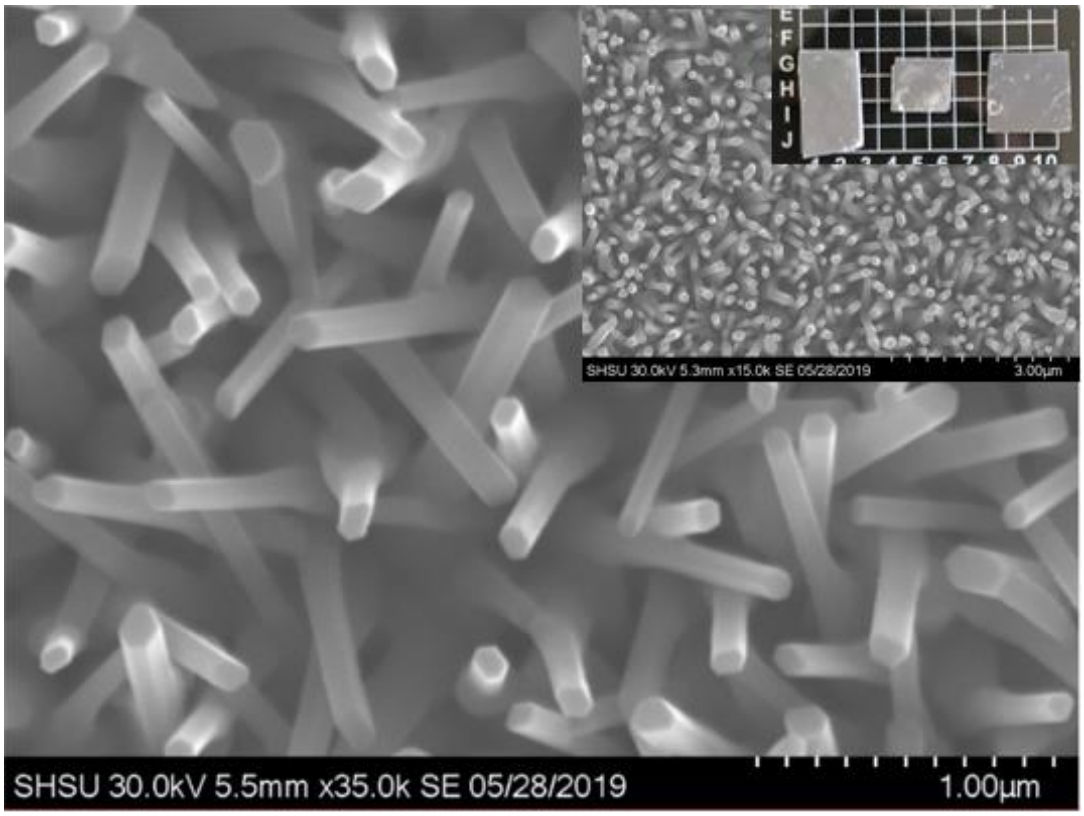

Figure 6. SEM image of undoped ZnO nanocolumns. Inset is an SEM image of the nanowires at half the magnification and an image of the entire substrate.

Several experiments took place under different reaction times to observe the influence on nanocolumn diameter (Figure 7). This is important to investigate as a smaller diameter of nanocolumns leads to more surface area per gram of product. Increased nanostructure surface area creates additional contact sites with the sensitizer, which could improve electrode performance in DSSCs. Reaction times were in 15-minute intervals starting at 30 minutes and ending at 105 minutes. A linear trend is apparent; as reaction time increases so does nanocolumn diameter. It is also important to note that the standard deviation also increases with reaction time. Diameters from 30 of the nanowires in each trial were measured to determine this trend.

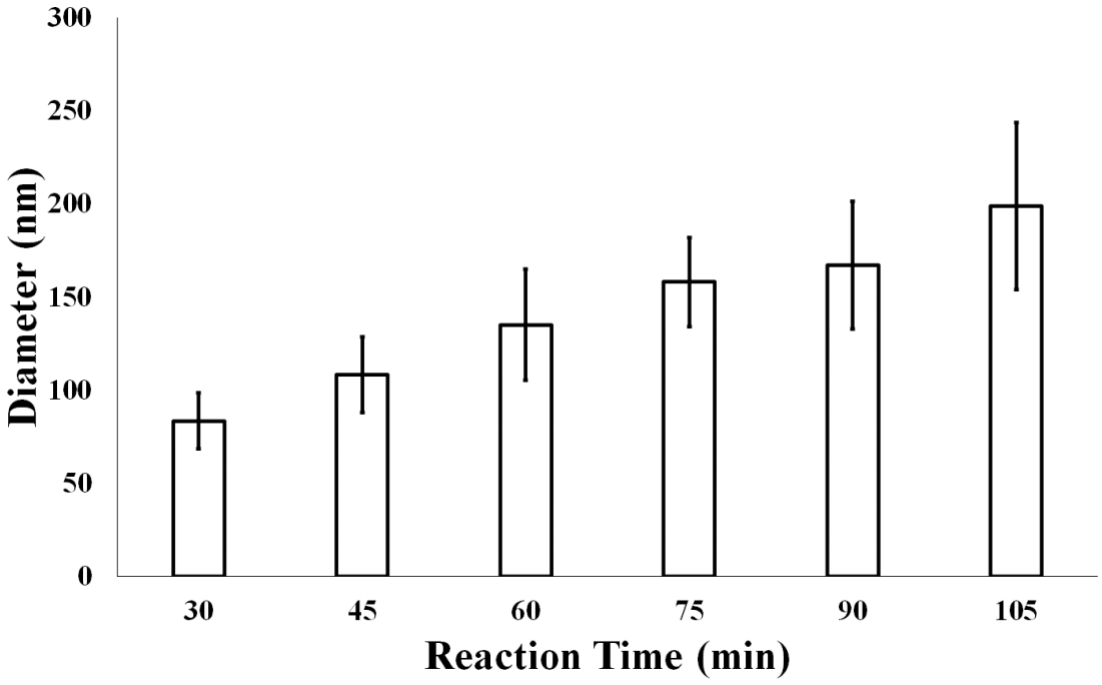

Figure 7. The effect of synthesis reaction time over nanocolumns' diameter.

Optical properties

Photoluminescence gives insight into the optical properties as well as the structural defects of nanomaterials. Room temperature photoluminescence spectrum of as-synthesized ZnO nanowires is shown in Figure 8. Wavelength indicates the type of transition that is happening, whether it be a band-to-band transition or the relaxation of a defect. Peak intensity correlates to the number of photons being emitted at a particular wavelength. The near-band edge (NBE) peak appeared at 380 nm as corroborated by the literature for similar structures.[39] Emission at this wavelength was used to calculate the band gap of the material using the energy equation below (Eq. 6).

$$E_g = \frac{hc}{\lambda} \quad (6)$$

The calculated bandgap of 3.26 eV appeared to be lower than literature values for bulk ZnO at 3.37 eV. The change in bandgap from bulk to nanomaterial is heavily influenced by the morphology of the material and heavily dependent on the aspect ratio.[40] The broadness of the NBE peak for the nanocolumns is inconsistent with literature, typically showing sharp NBE emission.[41] This could be due to the analysis performed at room temperatures, and the introduction of zinc vacancies (V_{Zn}) and zinc interstitials (Zn_i) within the structure.[42, 43] V_{Zn} have an emission peak at 405 nm and 437 nm. While Zn_i has an emission peak at 395, 440, and 455 nm. Zn_i are donors which contribute to the n-type semiconducting nature of ZnO, whereas V_{Zn} is quite the opposite being shallow level acceptors and contributing more to p-type semiconducting properties. The wide peak at 490 nm is indicative of oxygen vacancies (V_O) within the crystal lattice. These are deep-level donors, thus showing the n-type semiconducting nature of undoped ZnO. Although evidence of V_{Zn} contributing to p-type semiconducting properties exists, the structure showed a large amount of V_O consistent with the n-type nature of ZnO.

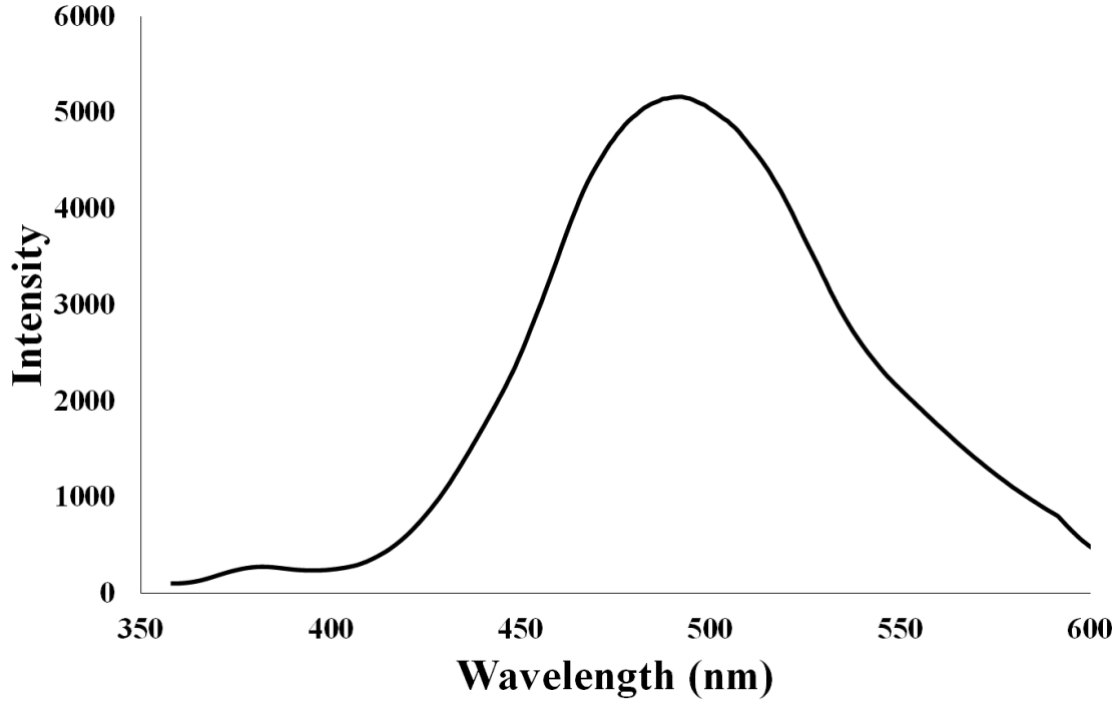

Figure 8. Room temperature photoluminescence of CVD grown ZnO nanocolumns.

Photoluminescence spectra of ZnO nanocolumns synthesized at varied reaction times are presented in Figure 9. The bandgap shifts from 3.25 eV to 3.20 eV when reaction time increases to 75 minutes and above, but then lowers to 3.22 eV at 105 minutes. The small shift in bandgap energies is due to the different aspect ratios of the nanowires, as mentioned earlier. The bandgap is calculated by converting the wavelength of the near band emissions peak to energy (Equation 6). Figure 10 is a representation of the band gap of ZnO. The near band emissions peak correlates to the fluorescence of photons that are relaxing from the conduction band to the valence band. The 45-minute reaction time trial shows an intense green emission peak that has a lower intensity than that of the 60-minute trial. Experiments conducted above the 60-minute reaction time show an evident linear trend. The intensity of the green emission peak decreases with increasing reaction time.

This can be interpreted as a decrease in oxygen vacancies and possibly other surface-level defects as reaction time increases.

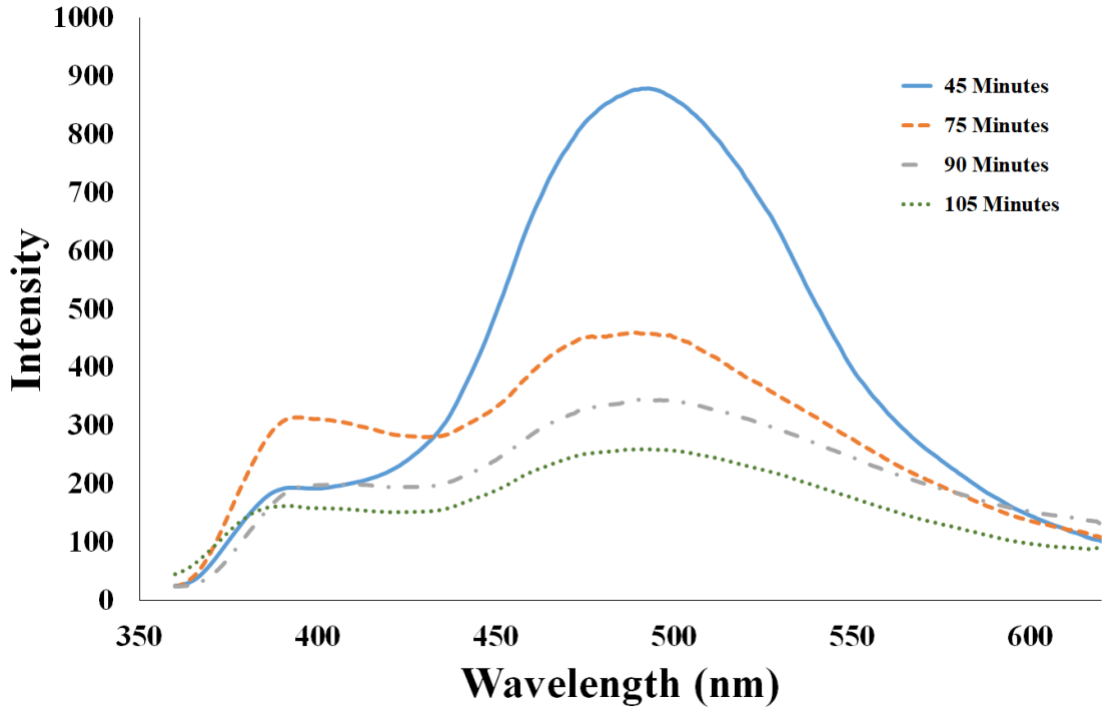

Figure 9. Room temperature photoluminescence of CVD grown ZnO nanowires at varying synthesis times.

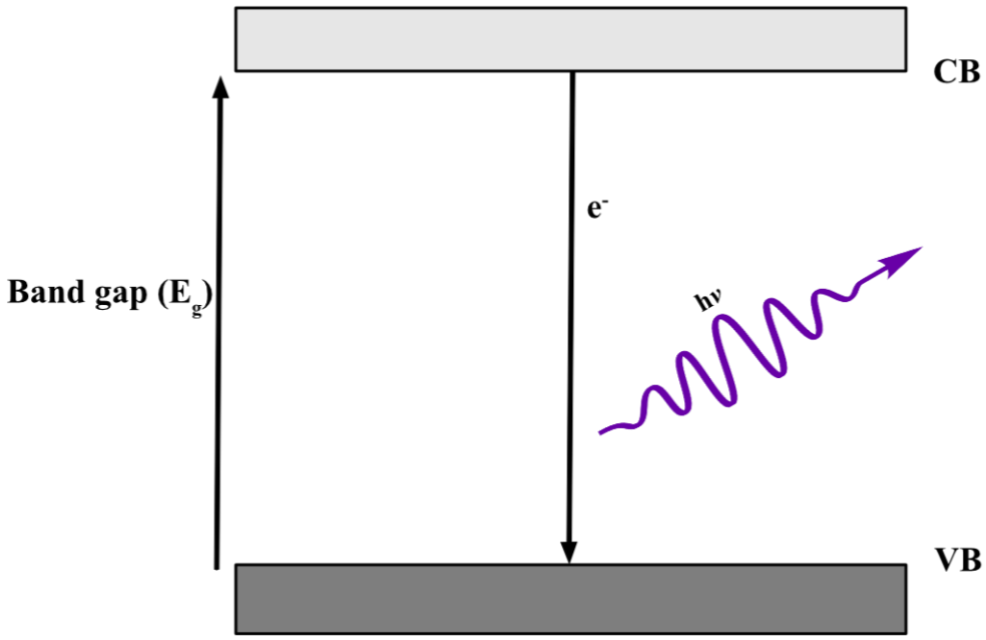

Figure 10. Representation of an electron relaxing from the conduction band to the valence band releasing a photon that is used to measure the band gap.

Conclusion

The synthesis of ZnO nanowires was achieved using a novel chemical vapor deposition method that utilized an inner reaction tube to promote ZnO richness at the substrates. The introduction of an inner reaction tube shows promise as an improvement to the CVD method that increases the uniformity and scalability of ZnO nanowires. The synthesized nanowires show no evidence of multiple crystal phases or impurities, thus showing improved crystal quality. Photoluminescence shows evidence of a large concentration of oxygen vacancies leading to n-type semiconducting properties. However, there is also evidence of Zn vacancies that are electron acceptors, giving rise to a slight p-type contribution. This could be advantageous when trying to synthesize p-type ZnO via doping as it will contribute to the overall semiconducting property of the material. The

influence of reaction time is obvious on both the diameter and the photoluminescent properties of the nanocolumns. PL data suggests a lower number of surface-level defects in larger nanocolumns. Consequently, and within the presented ranges of experimental conditions, tunability of the aforementioned nanocolumn properties was achievable.

CHAPTER III

The Comparison of Sb^{3+} and Sb^{5+} as Dopants for P-Type ZnO: Photoluminescence and Structural Analysis

Introduction

ZnO has proven to be a versatile semiconducting nanomaterial. Its direct wide bandgap (3.37 eV) and high electron mobility (60 meV) at room temperature make it an attractive material for many optoelectronic and photovoltaic applications. Thus, many have investigated the versatility of ZnO by synthesizing nanostructures using a variety of unique methodologies. An interesting property of ZnO is its intrinsic n-type conducting nature. The oxygen vacancies (V_O), zinc interstitials (Zn_i), and hydrogen impurities are the primary influencers in this semiconducting behavior. Due to this, the ability to produce p-type semiconducting ZnO has proven to be a challenge. Several studies show that ZnO can produce p-type semiconducting behavior by being doped with group 5 elements, such as N[44], P[45], As[46], and Sb[47]. The fabrication of low resistivity p-type ZnO has the potential to increase its versatility even further in optoelectronic and photovoltaic applications.

Doping ZnO is typically done by introducing a small amount of a dopant into the system during the reaction. The incorporation into the crystal lattice is dependent on the dopant and the method of synthesis. In ZnO, the dopant may replace one of the atoms and occupy the site. Another possibility is the interstitial incorporation of the dopant. Rather than replacing a Zn or O atom, the dopant is able to fit in between atoms within the crystal structure. Consequently, the incorporation of the dopant may also lead to an increase in another already present defect, or it may introduce new defects into the crystal. The replacement of Zn or O with a p-type dopant will remove electrons from the system;

forming shallow or deep level electron acceptors that transform the semiconducting nature of ZnO.[48]

Doping ZnO with early group 5 elements like N and P leads to the substitution of the O atom with the dopant. However, in the case of As and Sb, the situation is a bit more complicated. The atomic radii of As and Sb do not substitute O atoms. Instead, they replace the Zn atoms and form a X_{Zn} - $2V_{Zn}$ (X=Sb or As) acceptor complex. The large radius of antimony replaces a single Zn atom and prohibits the formation of other Zn sites leading to zinc vacancies. Antimony with an oxidation state of +3 interacts with two $(V_{Zn})^{2-}$ defects. Showing the overall complex as to having an oxidation state of -1. This can be interpreted as the donation of a positive charge carrier from a surrounding atom. Thus, having one less electron in the system overall. This is the reason for observing the p-type conductivity in Sb-doped ZnO. ZnO's inherent n-type conductivity and its self-correcting nature pose a problem for p-type doping.[49] This is the advantage of using antimony as a dopant. Antimony can produce a stable p-type ZnO material using straight-forward methods such as chemical vapor deposition or hydrothermal synthesis.[50,51]

This chapter is a study of two oxidation states of antimony, Sb^{3+} and Sb^{5+}, and their influence on ZnO as p-type dopants. The synthesis method described in chapter-3 was slightly modified and tested as a possible vapor phase doping mechanism. In addition, the influence of dopant nature and concentration on crystal structure, morphology, composition, and photoelectronic effects was studied.

Materials and Methods

ZnO nanoparticle synthesis

Three silicon substrates (Ted Pella, Inc – Si(100)) were cut into approximately 1 cm x 1 cm pieces. These substrates were sonicated in an ethanol (Sigma-Aldrich – 200 proof) bath for 10 minutes, followed by sonication in an acetone (VWR Chemicals – 99.5%) bath for 10 minutes before being dried under flowing nitrogen gas. A ZnO seed layer was prepared by coating the surface of the substrates with a 5.5 mM solution of zinc acetate (Sigma-Aldrich – 98%) and allowing it to evaporate completely. The substrates were then heat-treated in a 160 °C furnace for 45 minutes. This process was repeated once more with the same zinc acetate solution and heat-treated for 60 minutes rather than 45. A gold-covered (10 nm) silicon substrate (Platypus Technologies – AU.100.SLO) was also used as a substrate for synthesis. A 50 mg mixture consisting of a 6:1:2 mole ratio of Zn (Aldrich – ≥99%) to C (Aldrich - <20 μm, synthetic) to Sb_2O_5 (Alfa Aesar – 99.998%) or Sb_2O_3 (Alfa Aesar – 99.999%) was used as a precursor. A large Sb_2O_x mole ratio is necessary, as the temperature needed for the sublimation of Sb_2O_x temperature is lower than 950 °C at ~574 °C at 1 torr. Thus, a larger mole ratio will allow for some reduction of the Sb_2O_x to take place at 950 °C. This will allow for desired frequency of defects to ideally be between 0.5% and 2%. The precursor was placed at the bottom of a quartz reaction tube (1.2 cm i.d. x 25 cm) that had a single opened end. The prepared silicon substrates were placed at the mouth of the quartz reaction tube, in contact with one another, with the seed layer exposed. The quartz tube is then placed in the horizontal tube furnace (MTI Corporation – OTF-1200X) with the middle substrate aligned with a temperature zone of ~730 °C when the furnace is active, and the precursor aligned with the heating element

(center of the furnace). The reaction takes place at 950 °C (with a ramp time of 10 °C/min) with a reaction time of 60 minutes. An oil roughing molecular pump was used to achieve a pressure of 2.55 torr (MTI Corporation – PV-HVS2). Ar gas (Ultra-High Purity) was introduced into the system via a mass flow controller (MTI Corporation – GSL-3Z) at 80 sccm. After reaction completion, substrates were allowed to anneal and subsequently cool down to room temperature.

Nanostructure morphology, composition, and structural analysis

Nanostructure size and shape were analyzed using scanning electron microscopy. Elemental mapping was performed using energy-dispersive X-ray spectroscopy. Room temperature crystal phase and structural data were investigated using a Rigaku Miniflex 600 benchtop powder X-ray diffractometer. The 2θ values were observed from 20° to 65° with a current of 15 mA and a voltage of 40 kV. The crystal phase of the structure was identified and matched using the crystallography open database. Room temperature photoluminescence was analyzed using a Hitachi F-4500 Fluorescence Spectrometer. The excitation wavelength was set to 325 nm, and the scan went from 350 nm to 600 nm at 700V. The slit width for the excitation beam was 10 nm and 5 nm for the emission beam.

Results and Discussion

Structural analysis

X-ray diffraction was used to monitor indications of possible structural changes to the ZnO crystal phase as a result of doping (Figure 11). The undoped ZnO diffraction peaks are indicative of a hexagonal wurtzite crystal phase with 2-theta values and (h k l) planes respectively at 31.70 (1 0 0), 34.35 (0 0 2), 36.20 (1 0 1), 47.45 (1 0 2), 56.65 (1 1 0) and 62.85 (1 0 3). The (1 1 0) diffraction plane is low in intensity but still observable giving

rise to a typical wurtzite structure (COD # 1011258). The Sb-doped ZnO nanostructures show peaks at 31.80 (1 0 0), 34.45 (0 0 2), 36.30 (1 01), 47.60 (1 0 2), 56.65 (1 1 0), and 62.75 (1 0 3). Bragg's Law, or X-ray diffraction equation is presented below (Eq. 7).

$$n\lambda = 2d\sin\theta \tag{7}$$

Where n is an integer, λ is the wavelength of the x-ray, d is the spacing of the crystal lattice planes, and θ is the incident angle. Doping a different atom in place of another will likely change the d-spacing. However, shifts in diffraction planes may be difficult to discern. This small shift may primarily be due to dopants having larger or smaller lattice constants than that of the host atom. Such incorporation will increase strain on the crystal lattice and change the spacing of the crystal planes (d). The Bragg angle shift of the (1 0 0), (0 0 2), (1 0 1), (1 0 2), and (1 0 3) peaks is likely due to a smaller lattice constant that is consistent with Sb doping.[47]

Undoped ZnO nanowires exhibit sharp and intense (0 0 2) reflection which is indicative of a higher average volume of (0 0 2) crystal planes, thus an intense diffraction signal from such planes. However, the Sb-doped nanostructures exhibit a lower-intensity (0 0 2) peak owing to the reduced volume of such diffraction planes. Observable differences in XRD patterns could be a result of lattice mismatch between the grown structures and the catalytic seed layer (Au in this case). Otherwise, XRD patterns show no evidence of any other crystal phases or metal oxides being formed.

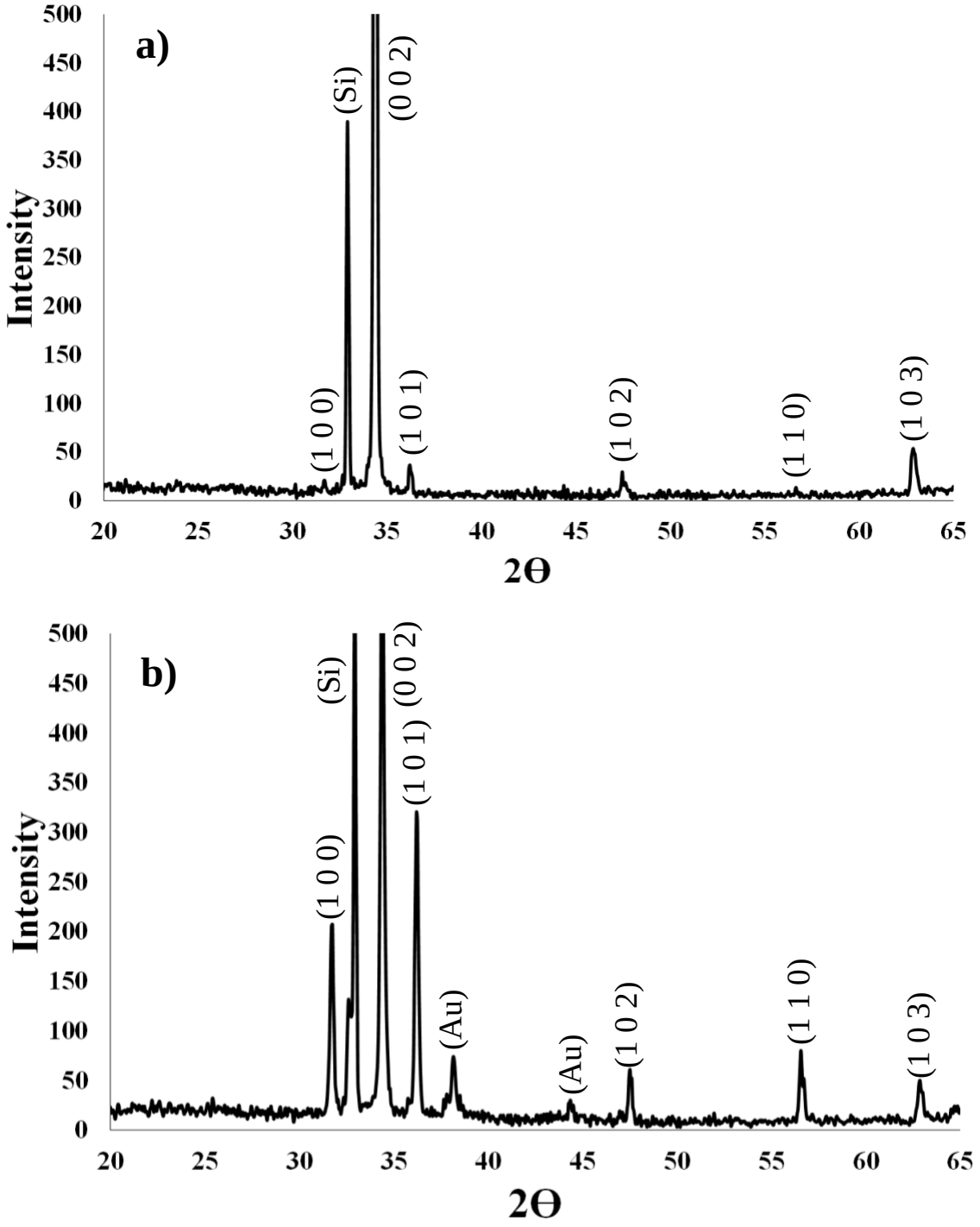

Figure 11. Powder X-ray diffractogram of a) undoped ZnO nanowires and b) Sb-doped ZnO nanowires.

Morphology and compositional analysis

The morphology of the ZnO nanostructures was observed using scanning electron microscopy (Figure 12). Undoped ZnO images show epitaxial growth from the substrate with diameters between 80 and 150 nm. The wires are hexagonal which is consistent with the typical wurtzite crystal phase of ZnO. The Sb-doped ZnO nanostructures show a larger wire-like structure with some epitaxial growth. However, there is much less uniformity and consistency in the growth pattern. There is also a noticeable increase in diameter of the doped structures with the diameters measuring 306 nm and 289 nm on average for the (b) Sb^{3+} and (c) Sb^{5+} trials respectively. The incorporation of the antimony and the defects it brings is most likely the cause of this change in consistency.

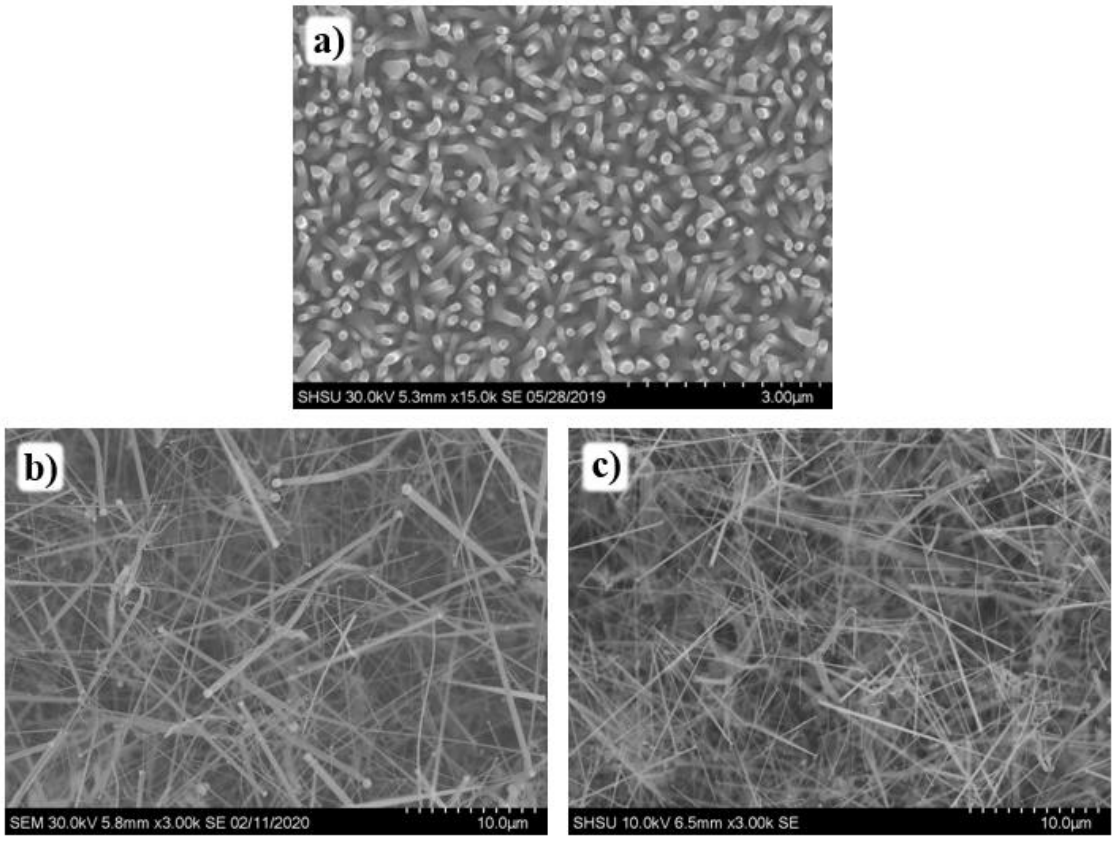

Figure 12. Scanning electron microscopy images of a) undoped ZnO nanowires, b) Sb-doped ZnO nanowires using Sb_2O_3 as dopant source, and c) Sb-doped ZnO nanowires using Sb_2O_5 as the dopant source.

The composition of the undoped and doped ZnO nanowires gives further insight into the structural and morphological effects of the antimony dopant (Table 1). EDS data shows atomic ratios of Zn to O in all three crystal structures to be ~ 1:1. More specifically 44.60%, 46.28%, and 43.86% Zn in the undoped, Sb(III) doped, and Sb(V) doped respectively. The other major element being oxygen at 55.40%, 53.39%, and 55.83%. This is further evidence of forming stoichiometric ZnO nanoproducts with no un-reacted zinc. The ratio of Zn to O does not change drastically from the undoped to doped structures raising questions as to the actual extent of doping achieved in the gas phase. The

incorporation of antimony does seem to have a dependence on the oxidation state of the starting material. Using Sb^{3+} as a starting material allowed for the total atomic percentage of antimony to reach 0.33%, while Sb^{5+} as a starting material incorporated 1.19% into the structure. Sb^{3+} has an ionic radius of 0.076 nm and Sb^{5+} has a radius of 0.061 nm. The smaller radius of the Sb^{5+} may allow for easier incorporation due to its smaller size. Another possible reason for this preference of incorporation is that Sb prefers to be in the Sb^{5+} oxidation state when it is doped into the structure.[47,52] This does pose a problem for p-type conductivity, however, since the main proponent of the expressed p-type conductivity comes from the Sb_{Zn}-$2V_{Zn}$ complex, the fact that Sb^{5+} is a pentavalent species contradicts this. As mentioned earlier, the Sb_{Zn}-$2V_{Zn}$ complex expresses p-type conductivity because the Sb atom is donating 3 electrons and zinc vacancies accept two electrons each, leaving an excess hole. If this were the pentavalent species (Sb^{5+}) then an extra electron would be present resulting in n-type conduction. This doesn't mean that p-type conductivity isn't expressed, rather the nature of the p-type conductivity is not completely solved. Further investigation of this phenomenon is needed since there is no current conclusive mechanism in the literature describing the true nature of antimony doping and the kind of conduction it expresses.[53,54]

Table 1. Atomic percentages of undoped and Sb-doped ZnO nanowires measured via EDS

Dopant	*Zinc*	*Oxygen*	*Antimony*
None	44.60%	55.40%	N/A
Sb^{3+}	46.28%	53.39%	0.33%
Sb^{5+}	43.86%	55.83%	1.19%

Optical properties

Room temperature photoluminescence was used to investigate the optical properties of the CVD grown Sb-Doped ZnO nanowires (Figure 13). Typical with ZnO nanostructures, two peaks are present. The first is a near-band emission (NBE) peak at around 379 nm for undoped ZnO, 398 nm for Sb^{3+}-doped ZnO, and 397 nm for Sb^{5+}-doped ZnO. The expression of this peak gives insight into the bandgap of the structures. At 379 nm the bandgap of undoped ZnO is 3.27 eV. When doped with Sb the overall bandgap is lowered to ~3.12 eV. The lowering of this bandgap is consistent with typical Sb doping.[55] The intensity of the NBE peak is a determinant of e^--h^+ pair lifetimes. A decrease in intensity is an increase in lifetimes.[56] Another possibility of a less intense peak could be due to lower ZnO density, which would lead to less electrons in the material. Since the intensity of the peak is reliant on the relaxation of electrons to emit photons, having fewer electrons would release fewer photons. Both Sb-doped nanostructures show an increase in NBE peak intensity thus having a shorter e^--h^+ pair lifetime.

The peak in the 500 nm region gives information on the structural defects of the crystals. The primary contributor to this peak is the V_O defect which is typical for ZnO. The most notable characteristic of this defect is the fact that it is a deep-level electron donor. As mentioned before, this is the primary reason for ZnO's inherent n-type nature. A decrease in this peak could suggest fewer defects in the lattice. The undoped ZnO has the most intense green emission peak of the three trials. However, Sb^{3+} is still showing a high intensity of this peak, which can be assumed to be the expression of many V_O defects. While Sb^{5+} is showing much lower intensity compared to the other two. The argument could be made that the structures are smaller and possibly less dense than that of the other

two substrates, which is leading to a decrease in the amount of V_O defects. However, the NBE peak is proportionally larger than the other two trials, which supports the idea that a lower crystal density is not the case. The green peak of undoped ZnO has an apex at 490 nm. The apex of Sb^{3+} is red shifted to 497 nm. The most likely reason for this is the convolution of multiple peaks in this region. Multiple defects are expressed between 400 and 500 nm.[43] The most notable ones in this region are V_{Zn} (405 nm and 437 nm) and Zn_i (440 – 455 nm). This red shift could be evidence of fewer V_{Zn} and Zn_i defects. To understand the true nature and structure of these crystals further investigations would be necessary.

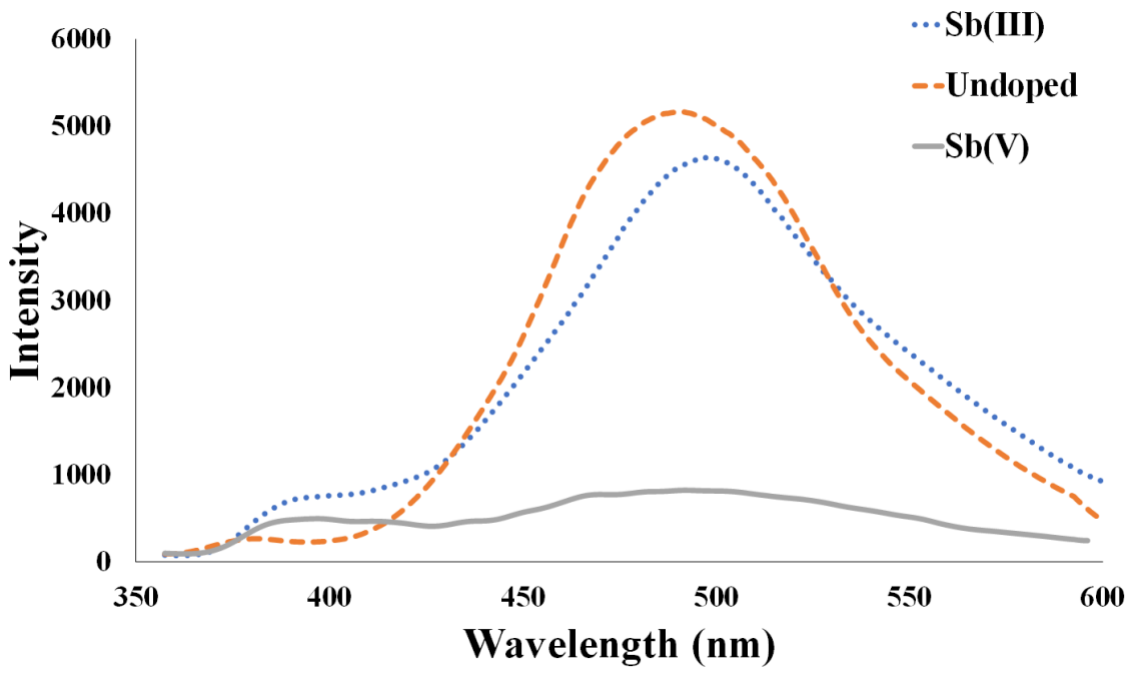

Figure 13. Room temperature photoluminescence of undoped, Sb(III) doped, Sb(V) doped ZnO.

Conclusion

The Sb-doped ZnO structures were grown in the wurtzite crystal phase using a modified CVD method described in chapter-2. Powder XRD patterns with slight Bragg angle shift (0.1 to 0.15°) could, with conservation, point to Sb doping. No evidence was obtained of the formation of any crystal phases other than Wurtzite ZnO. Photoluminescence data suggested a shorter e^--h^+ lifetime and decreased bandgap for Sb doped ZnO structures. The Sb^{3+} doped structures exhibited a small decrease in oxygen vacancy defects but were not significant enough to shift the n-type nature of ZnO to that of a p-type semiconductor. The Sb^{5+} doped structures show a large decrease in the expression of these defects which means a decrease in n-type nature. Relevant literature show promise to use Sb-doped ZnO for p-type DSSCs, however, additional studies are needed to understand the true nature of this material and its use in photovoltaic devices.

CHAPTER IV

The Effects of Increasing Cu^{2+} Doping on Morphology and Electron Mobility of Zno for Dye-Sensitized Solar Cell Applications

Introduction

Similar to the previous chapter, this study focuses on the synthesis of p-type ZnO using an electron-deficient dopant. To reiterate, the purpose of this is for the eventual use in Grätzel type dye-sensitized solar cells (DSSCs) in hopes to increase the performance of these devices. P-type ZnO has been considered much more recently as potential working electrode material rather than n-type ZnO. The reason for this is because n-type ZnO DSSCs are still being outperformed by TiO_2 DSSCs with these devices having max efficiencies of 8% and 13% respectively.[32,34] The lack of efficiency has been attributed to two reasons. The first is the formation of Zn-dye aggregates that promote recombination and decrease electron mobility.[57] The other issue is the lower density of state (DOS) in ZnO when compared to TiO_2.[37] The dye issue is not necessarily fixed by using p-type ZnO over n-type ZnO. However, the lower density of states can be combatted by using p-type ZnO since the path of the electron in p-type DSSCs flows through the valence band of the metal oxide rather than the conduction band.[58] The DOS refers to the available levels in the conduction band or just below the conduction band that an electron can occupy. Thus, having a lower DOS leads to fewer available levels for electrons from the sensitizer to occupy. ZnO shows exceptional electron mobility, but it is bottlenecked by low DOS. This solves the problem of the DOS bottleneck and has the potential to further the development of ZnO-based DSSCs.

Copper has seen much success as a p-type dopant in ZnO nanowires due to its favorable properties and ease of incorporation.[59,60] Cu has two oxidation states of Cu^{1+} and Cu^{2+}. The ionic radii of these two different oxidation states are 0.077 nm and 0.073 nm respectively. Since Zn has an atomic radius of 0.074 nm, copper can replace a Zn atom rather easily.[61] The nature of the p-type conductivity comes from the substitution of the Cu atoms with Zn. This is due to Cu having 1 less electron in its valence shell giving the system excess of holes. Copper also forms surface-level acceptors increasing positively charged carriers. Copper and other metal dopants (Mg, Ag, Ni, etc.) have been shown to increase electron mobility and suppress recombination.[62] The increase in electron mobility and overall efficiency is due to the shortening of the bandgap, which would allow a larger range of photons to be absorbed.[63] Cu has another advantage of being able to form oxides on the surface of ZnO acting as a barrier layer preventing the formation of Zn-dye aggregates.[64]

This work focuses on the synthesis of Cu-doped ZnO using vapor phase transport. This chapter also investigates the structural, morphological, and optical effects of increasing concentrations of Cu dopant in ZnO nanowire synthesis. Understanding the change in bandgaps and surface-level defects may help answer questions related to conductivity modification as a result of Cu doping. Not only is this an investigation of the Cu-doped ZnO it is also an opportunity to understand the limitations of our CVD method towards gas-phase doping of such metal oxide nanostructures.

Materials and Methods

Fabrication of Cu-Doped ZnO nanostructures

A mixture of ZnO (Goodfellow – 99.999%), graphite (Aldrich - <20 µm, synthetic), and CuO (Aldrich – 99.99%) was prepared with a 1:0.5:0.001 mole ratio as the precursor.

CuO is used as a precursor as it will reduce in the presence of carbon at temperatures above 600 °C. Synthesis of Cu-doped ZnO structures was attempted identically as to that described in chapter 2 (page 13).

Room-Temperature photoluminescence

Room temperature photoluminescence was performed using a Hitachi F-4500 Fluorescence Spectrometer. The excitation wavelength was 325 nm, and the scan was from 350 nm to 600 nm at 700V. The slit widths were 10 nm for the excitation beam and 5 nm for the emission beam.

Morphology and composition

The nanoparticles morphology was looked at using scanning electron microscopy (SEM). The composition of the nanostructures was characterized using energy-dispersive X-ray spectroscopy (EDS).

X-Ray diffraction

The crystal phase of the nanostructures was identified using a Rigaku Miniflex 600 benchtop X-ray diffractometer at room temperature. The 2θ values were scanned from 20° to 65° with a current of 15 mA and a voltage of 40 kV. The crystallography database was used to identify the crystal phase of the structures.

Results & Discussion

Structural properties

The crystal structure and phase of undoped and Cu-doped ZnO nanowires grown by vapor phase transport were investigated via powder XRD (Figure 14). These nanowires express crystallographic characteristics that are indicative of a wurtzite crystal phase with

an intense (0 0 2) peak at 34.45°, a (1 0 0) peak at 31.7°, a (1 0 1) peak at 36.2°, a (1 0 2) peak at 47.45°, and a (1 0 3) peak at 62.85°. There are no other peaks in the diffractogram, indicating the absence of any other crystal phases like zinc blende or a CuO-related structure. There are no observable shifts of reflections. The lack of a Braggs angle shift suggests that the Cu^{2+} ions (0.073 nm), instead of the Cu^{+} ions (0.079 nm), may have been incorporated into the crystal structure possibly replacing the Zn (0.074 nm).[65] Compositional studies via EDS confirmed the presence of Cu within the lattice. Increasing concentrations of copper in the precursor (to a certain extent) does not have a drastic impact on the relative intensity of the diffractions. This could be an indication of the lack of a noticeable impact on the morphology of the nanowires.

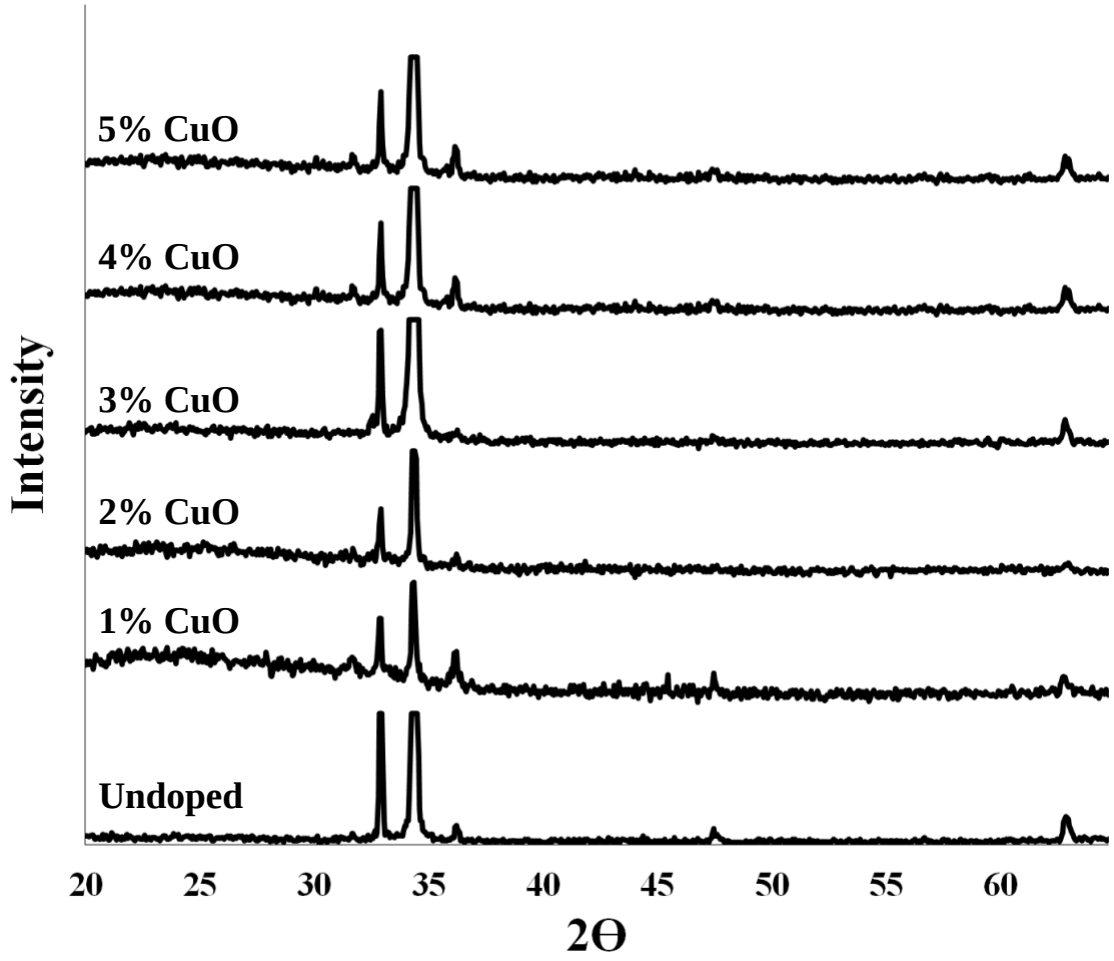

Figure 14. Powder X-ray diffractogram of undoped and Cu-doped ZnO nanowires at select concentrations of CuO precursor.

Morphological and compositional studies

The morphology of the undoped and Cu-doped ZnO nanowires was investigated using scanning electron microscopy (Figure 15). The morphology of the two structures is uniform and can be described as hexagonal nanowires with epitaxial growth from the substrate. The inset of Figure 15 displays the nanostructures on a larger scale, this confirms that doping with copper does not hinder the uniformity of the ZnO nanowires. The influence of increasing amounts of copper dopant on the diameter of the nanowires is

shown in Figure 16. Undoped nanowires have an average of 135 nm. The Cu-doped nanowires have an average diameter between 80 and 110 nm. There's no obvious correlation between the amount of CuO used in the precursor and the diameter, except for the initial incorporation from 0% to 1% copper where the overall decrease was ~55 nm. Concentrations above 1% are neither consistently increasing nor decreasing. The overall decrease in diameter is most likely due to a decrease in bond length between the Zn and O, which has been seen by other researchers in the field.[66] This compacts the crystal structure and shrinks the diameter of the doped nanowires. However, a change in bond length would most likely show a shift in the Bragg angle, which was not seen in the XRD investigations (Figure 14). Another possibility for this change in size may be due to a change in reaction parameters. An increase in oxygen in the system from the CuO or inconsistent seed layer deposition may be the cause for this change in nanowire diameter. Further investigations would be needed to better understand what is happening. The nanowires that were doped with a 5% CuO precursor are noticeably smaller on average. This may be a consequence of the over-saturation of Cu or O in the system that is preventing the growth of ZnO rather than reducing bond lengths or tightening the structure.

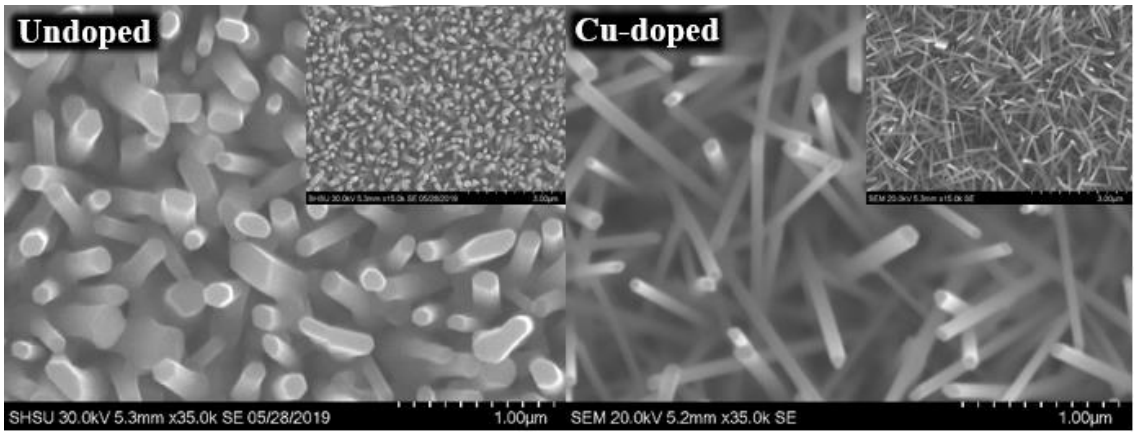

Figure 15. SEM images of undoped and Cu-doped nanowires.

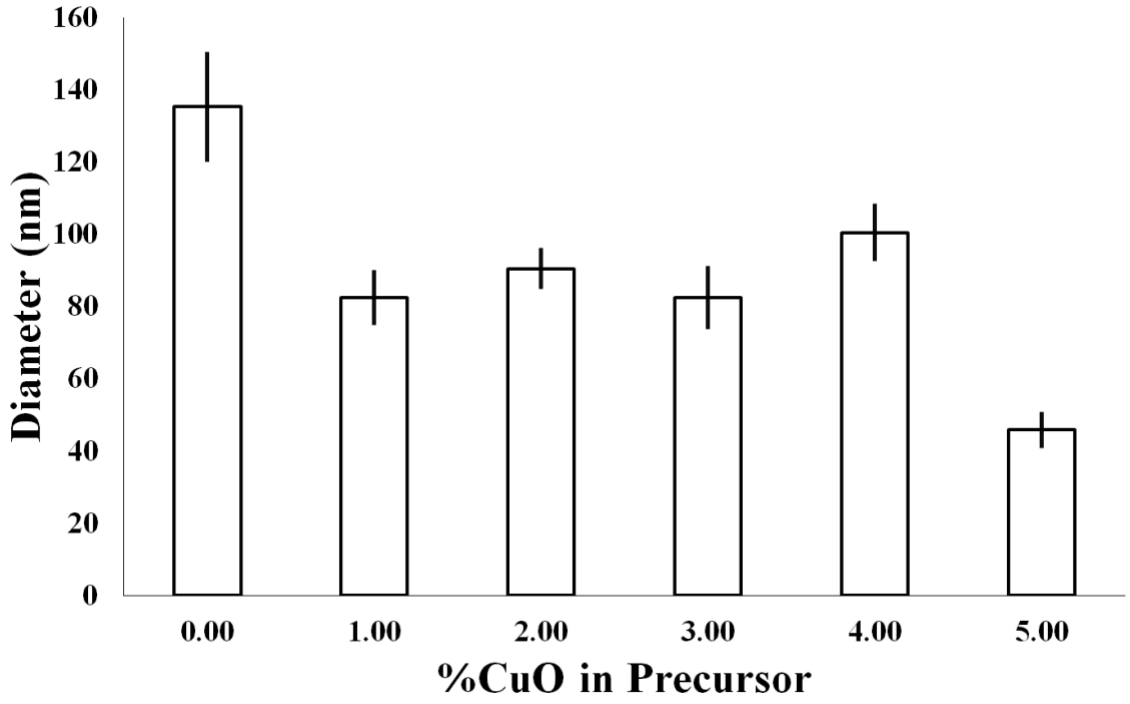

Figure 16. The diameter of ZnO nanowires with increasing amounts of CuO in the precursor. Measurements were taken from 30 nanowires from the SEM images from each of the samples.

Energy-dispersive X-ray spectroscopy was used for elemental mapping of the undoped and doped ZnO NWs (Table 2). The atomic percentages of Zn and O are close to 50% of the composition, which is indicative of the formation of ZnO. The amount of copper dopant in the nanowires increased linearly, 1.11% - 1.71%, with increasing the amount of CuO in the starting material up to 4%. When the precursor reaches 5% CuO, the atomic percentage of the Cu in the nanowires is much lower at 1.21%. There are no clear reasons to explain this data, however, different factors such as dopant saturation, doping kinetics, and dopant access to lattice may be responsible for inhibiting structure growth and ultimately dopant uptake. The elevated strain on the ZnO crystal structure as the number of Cu ions oversaturates the system, may also inhibit further incorporation.

Table 2. The atomic percentages of Zn, O, and Cu of undoped and Cu-doped ZnO nanowires were analyzed by EDS.

CuO% in Precursor	*Zn (Atomic %)*	*O (Atomic %)*	*Cu (Atomic %)*
0	44.60	55.40	N/A
1	54.90	43.99	1.11
2	45.86	52.84	1.30
3	50.80	47.70	1.50
4	53.97	44.31	1.71
5	49.83	48.95	1.21

Optical properties

Room temperature photoluminescence spectra of undoped and Cu-doped ZnO nanowires are shown in Figure 17. A typical green emission peak at 496 nm was observed for the undoped nanowires, while the doped samples that used a CuO precursor at 1%, 2%, 3%, 4%, and 5% have peaks within the 482 – 501 nm range. The origin of this peak comes from oxygen vacancies within the crystal lattice. This is common with ZnO nanostructures. A less defined peak is observed in the near-UV region at 389 nm for the undoped nanowires and 396 nm for the Cu-doped nanowires. The intensity of these near-band emissions correlates to the e^--h^+ lifetime.[56] A noticeable decrease is apparent in this NBE peak for all of the Cu-doped nanowires. Confirming longer e^--h^+ lifetimes and the reduction of recombination. The resolution of this peak is most likely affected by additional defects within the crystal structure. An agglomeration of the various ZnO defects and their transition wavelengths was put together by Vempati and coworkers.[43] Based on this, two defects are most likely causing this lack of resolution. The Zn_i to V_{Zn} transition at 395 nm and the conduction band to V_{Zn} transition at 405 nm.[67,68] These defects influence the

conductivity of the material. V_{Zn} is a surface level acceptor (p-type) and Zn_i is a deep level donor (n-type). The red shift in the UV peak of the Cu-doped nanowires is indicative of a reduction in the bandgap (3.18 eV – 3.13 eV) from the doping of Cu.[69]

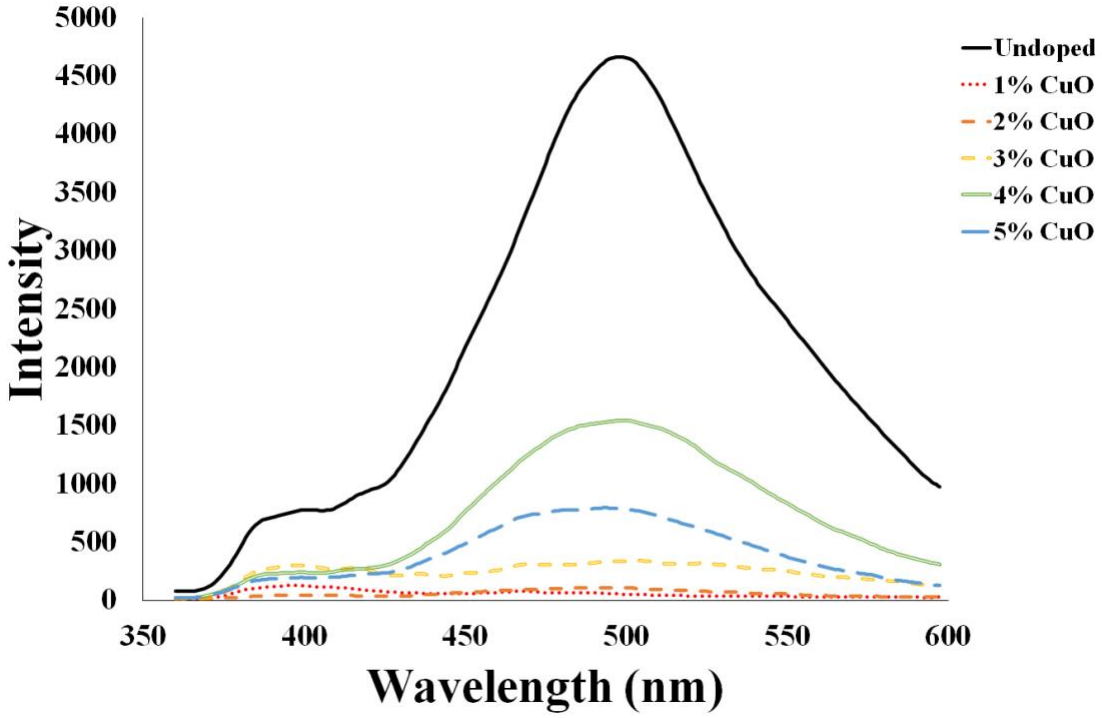

Figure 17. The room temperature photoluminescence spectra of undoped ZnO compared to Cu-doped ZnO that used increasing concentrations of CuO in the precursor.

Conclusion

Cu-doped ZnO NWs with increasing concentrations of Cu were synthesized using a novel CVD method. The method shows uniform growth and large substrate coverage. The diameter of the nanowires is lowered from 135 nm to under 100 nm when Cu is introduced into the crystal lattice. The photoluminescence data suggests that the undoped

ZnO nanowires have additional defects that are atypical in most ZnO nanostructures. The expression of these defects is evidence of p-type conductivity not only in the doped structures but in the undoped ones as well. The addition of Cu shows a decrease in the optical band gap by 0.05 eV. Along with the decrease in bandgap is evidence of a longer e^--h^+ lifetime, thus reducing recombination. The synthesis of Cu-doped ZnO nanowires using the novel CVD process presented here has the potential to increase the efficiency of ZnO-based p-type DSSCs.

CHAPTER V

Fabrication of ZnO based Dye-Sensitized Solar Cells

Introduction

The photovoltaic effect is a phenomenon that utilizes the unique properties of semiconductors to absorb a photon and form e^--h^+ pairs. The original photovoltaic cell was a p-n heterojunction cell that was fabricated by placing two pieces of silicon of different conductive nature together to form a grain boundary.[19] The grain boundary allows for an area of no net charge and the separation of electrons and their holes. The photovoltaic cell has evolved in several different ways. The p-n heterojunction cells are still being studied and employ a variety of different semiconductors/materials to improve the original design. Modern cell designs include metal oxide,[70] perovskite,[71] and dye-sensitized solar cells.[72]

Dye-sensitized solar cells use one semiconductor. Instead of forming a grain boundary between a p-type and n-type semiconductor, DSSCs utilize a dye to inject or sensitize an electron into the conduction band of an n-type semiconductor. This allows the flow of electrons to pass through the working electrode to an external circuit, which will encounter the counter electrode. The counter electrode facilitates electron flow into an electrolyte to reduce it. A more detailed description of DSSCs was presented in chapter I.

DSSCs can alternatively use p-type semiconductors rather than n-type. This reverses the flow of electrons completely (Figure 18).

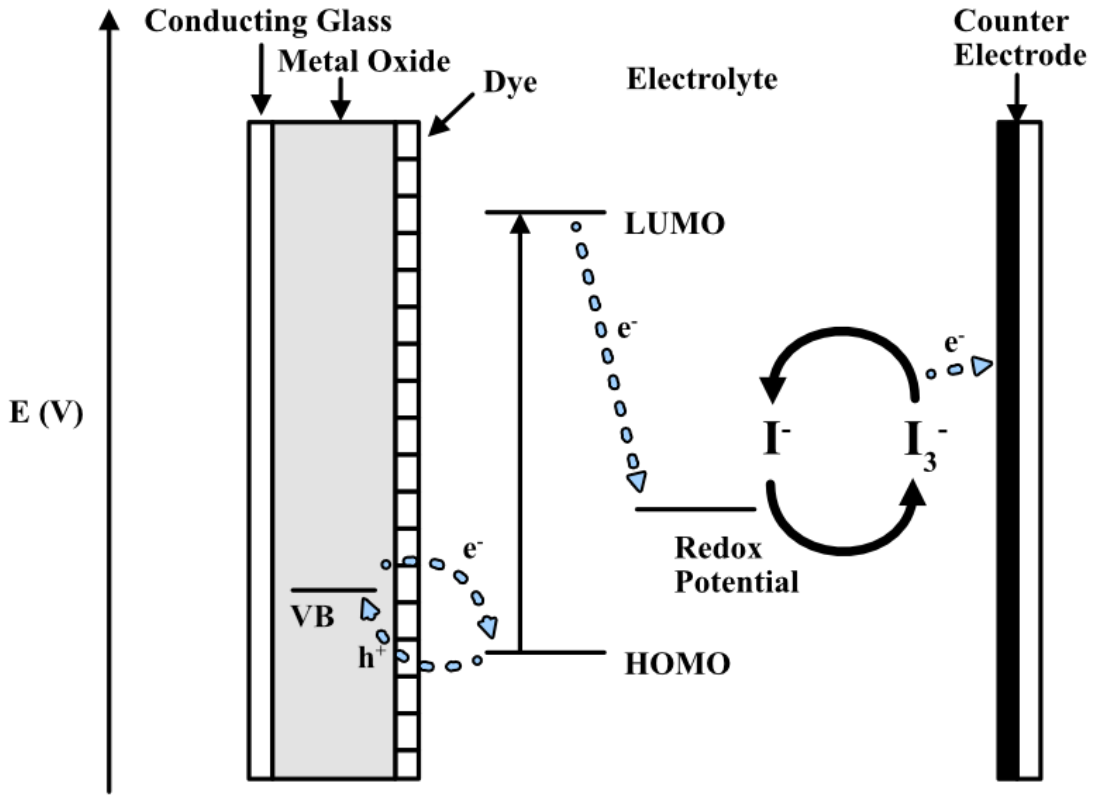

Figure 18. The flow of electrons through a p-type dye-sensitized solar cell.

The dye is still excited by absorbing a photon. Rather than injecting the electron into the conduction band of the semiconductor, it will instead reduce the electrolyte. The electron from the electrolyte flows through the counter electrode to an external circuit and contacts the working electrode with the p-type semiconductor. The electron fills a hole in the valence band rather than occupying a state in the conduction band. The electron is then donated to the dye to regenerate it. The reason for using p-type semiconductors over n-type is dependent on the properties of the semiconductor. For example, TiO_2 is the original metal oxide used for DSSCs and it is an n-type semiconductor with a direct wide bandgap (3.2 eV), electron mobility of 0.1 $cm^2 V^{-1} s^{-1}$, and achieved an efficiency of ~13% in 2014.[34] ZnO, on the other hand, is also an n-type semiconductor with a direct wide bandgap (3.37

eV) and superior electron mobility (205 $cm^2\ V^{-1}\ s^{-1}$), but has only achieved an efficiency of 8.22% in 2018.[32] ZnO is cheaper and has on par if not better relevant properties than TiO_2, so it makes sense to investigate ZnO for this application. However, n-type ZnO does not perform as well as TiO_2 which is why a spike in popularity for p-type ZnO has been seen in recent years.

The reason n-type ZnO performs poorly is due to its low density of states. P-type ZnO has the same issue in addition to being unstable, however p-type DSSCs do not use the conduction band of the metal oxide. Instead, they use the valence band.[58] This circumvents the problem and has the theoretical potential to outperform n-type ZnO and possibly TiO_2 as well. There are still a couple of challenges that p-type ZnO needs to overcome to perform better. V_O and O_i are both common defects in ZnO that are deep-level electron donors.[73] When doped with a potential p-type dopant, although the dopant is expressing p-type conductivity, ZnO tends to self-compensate by forming more of these deep-level donor defects. Furthermore, accidental doping of H^+ will also lead to increased n-type conductivity.[38]

The problem of the formation of Zn-dye aggregates has been combatted by using barrier layers to prevent this. The barrier layer is typically a highly conductive metal that will allow electrons to permeate it rather easily. The challenge of self-compensation and overall stability has been addressed by looking at different p-type dopants and their effectiveness. Accidental hydrogen doping is easily prevented by using a physical synthesis method and removing hydrogen from the system during the reaction and annealing stages. This problem primarily shows up in chemical-based methods as removing all the hydrogen from the system would be a near-impossible task.

This chapter focuses on the fabrication of p-type ZnO dye-sensitized solar cell prototypes using materials and methods described in earlier chapters. Resistance and conductivity were measured using a voltameter. Photovoltaic conversion efficiencies were measured using a solar simulator/potentiostat system.

Materials & Methods

Working electrode

A 1 cm x 2 cm substrate (Ted Pella Inc. – Si(100)) was sonicated and washed following previously described methods in this work. ZnO nanowires were now grown on the substrate using the CVD method discussed previously. An indium tin oxide (ITO) solution was prepared by dissolving 5 g of tin(IV) chloride (Acros – 98%) in 5 mL of methanol (Aqua Solutions – Reagent Grade). The solution was added to 4 mL of a solution containing 0.1 g of indium(III) nitrate (Aldrich – 99.98%) in 17 mL of methanol (Aqua Solutions – Reagent Grade) and 3 mL of HCl (Mallinkrodt – 37%). The ZnO nanowires were then carefully masked using a piece of silicon or another heat-resistant material large enough to cover 90% of the nanowires. Exposing about 2 -3 mm of nanowires that are touching the bare part of the silicon substrate. This is to allow the ITO layer to make direct contact with the ZnO nanowires. The substrate with the mask is placed into a furnace at 620 °C for 5 minutes. The substrate is removed from the furnace and the ITO is sprayed onto the exposed surface of the substrate for several seconds using an atomizer. The substrate is then placed back into the furnace for 150 seconds. This process was repeated once more. The substrate was allowed to cool to room temperature before further cell fabrication steps.

Counter electrode

A 1 cm x 2 cm quartz substrate (Advalue Technologies – FQ-S-001) was sonicated in 20 mL of ethanol for 10 minutes followed by sonication in 20 mL of acetone for 10 minutes. An ITO layer was applied to one side of the quartz using the process described in the working electrode. A 1 cm x 2 cm strip of copper tape was cut and cleaned by a quadruple sonication in 10 mL of hexane (Fluka – 99%), 10 mL of ethanol, 10 mL of acetone, and 10 mL of citric acid (Fisher – 99.9%) for 10 minutes each. The copper tape was then briefly washed in DI water. The copper tape was wrapped around half of the quartz piece.

Dye

A 0.9 mM solution of cis-Bis(isothiocyanato)bis(2,2'-bipyridyl-4,4'-dicarboxylato)ruthenium(II) (Aldrich – 95%) in acetonitrile (Aldrich – 99.93%) was prepared and stored in a 100 mL amber bottle.

Electrolyte solution

0.127 grams of iodine (Mallinckrodt) and 0.83 grams of potassium iodide (Aldrich) were dissolved in 10 ml of ethylene glycol (BDH – 99%) and stored in a 100 mL amber bottle.

Dye-Sensitized solar cell fabrication

The working electrode is placed in a beaker and the dye is added to completely cover the electrode. The beaker is then covered and stored in a dark cabinet for 12-24 hours. The electrode is then removed and allowed to dry. A small amount of silicone sealant is placed around the ZnO nanowire portion of the electrode and forms a small well. A drop of electrolyte is placed in the well. The copper portion of the counter electrode is placed

onto the sealant and is clipped together with the working electrode to allow the sealant to dry. The cell was then tested using a solar simulator (G2V Optics – Pico).

Results & Discussion

This ITO layer in the fabricated DSSC prototype was tested for conductivity (Figure 19), where resistance is inversely proportional to the conductivity (Eq. 8). The conductivity equation is expressed below where σ is the conductivity, R is the resistance, A is the area of the material, and l is the length between the clips. Although, the area of the material and the length between the clips varies slightly it is presumably not enough of a difference to greatly affect the conductivity that is being calculated.

$$\sigma = \frac{l}{RA} \tag{8}$$

Figure 19. The resistance of the ITO layer on the working electrode for a DSSC.

The N3 dye was absorbed on the surface of the ZnO nanowires by immersing the substrate in a dye bath overnight. The dye is visually adsorbed to the surface of the ZnO nanowires (Figure 20). However, a significant portion of the nanowires seemed to dissolve into the dye solution. The reason for this may be due to the N3 dye being acidic and extended periods of exposure may facilitate the solvation of ZnO. The dye adsorption needs to be optimized further to maximize the amount of dye adsorbed to the surface of the electrode while minimizing the amount of ZnO that is dissolved during the adsorption process. Alternatively, using a different dye is an option as chlorophyll, chlorophyll derivatives, and other natural dyes have shown to be effective sensitizers.[74,75]

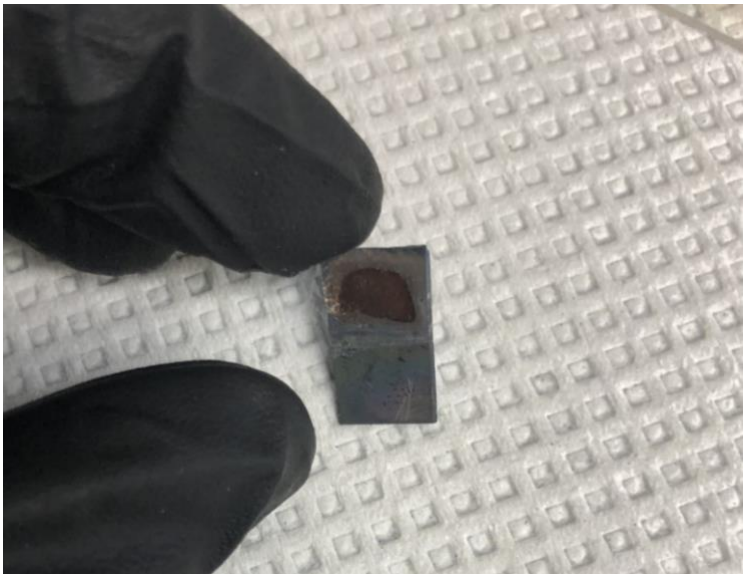

Figure 20. N3 dye adsorbed to the working electrode of a DSSC.

The counter electrode composed of a quartz substrate with a layer of ITO on the surface had its conductivity measured using a voltmeter (Figure 21). The resistance measured out to be 26 Ω. Using the relationship of resistance to conductivity (Equation 8) the conductivity would be comparatively high to the working electrode (Figure 19).

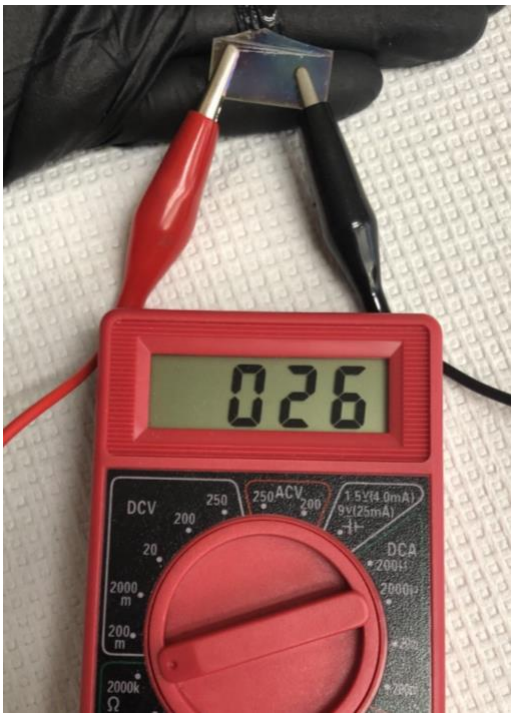

Figure 21. The conductivity of the ITO-covered quartz counter electrode.

Photovoltaic conversion efficiency investigation

The photovoltaic conversion efficiency of the fabricated cell was measured using a G2V solar simulator (1.0 Sun) and a silicon reference solar cell as a standard (Figure 22). The parameters for this test were preloaded onto the instrument. This measurement also took place under a simulated air mass of 1.5, which is standard for representing the spectral composition on earth. The IV curve is typical of a photovoltaic cell. The PCE of the reference cell was measured to be 18.05%, 1.937 V for the V_{OC}, 11.95 mA for the I_{SC}, and 74.46% for the fill factor. It is appropriate to note that this reference cell is connected directly to the solar simulator rather than using clips or probes, which could lead to errors in measurements.

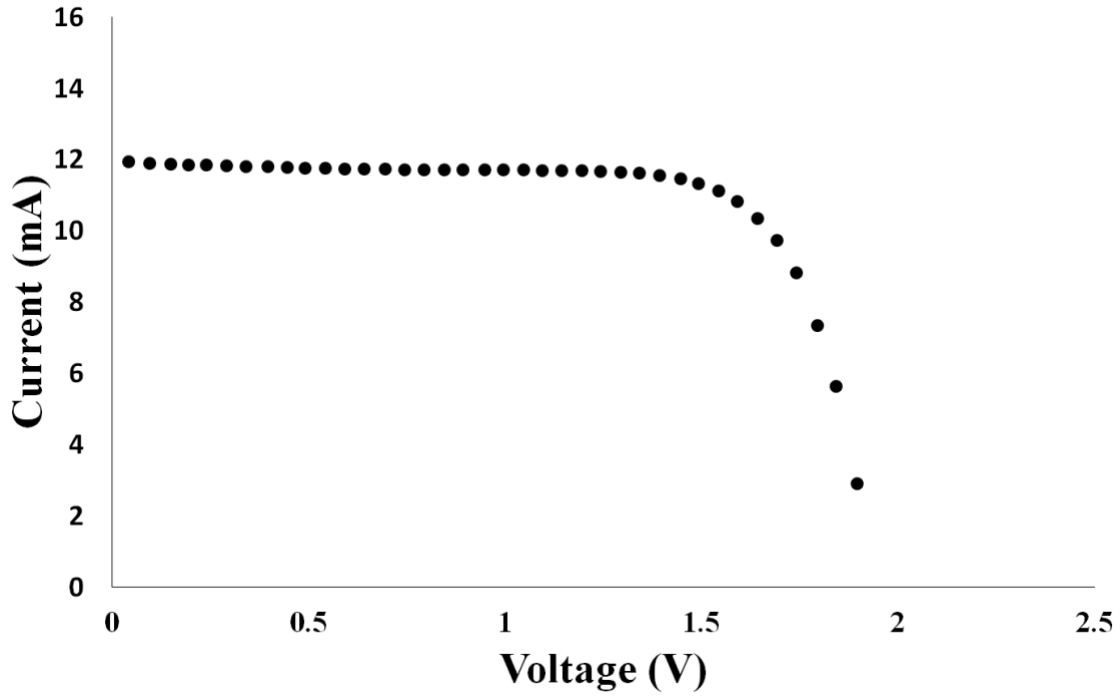

Figure 22. The IV curve of a G2V silicon reference solar cell at AM 1.5.

Current/voltage (I/V) measurements of the fabricated DSSC (Figure 23) were typical of a diode rather than a photovoltaic cell and no measurable PCE was recorded (Figure 24). Thorough testing of individual components including dye, electrolyte, sealant, and electrodes is necessary to identify the problem/s. The electrolyte and dye used have proven to work extensively in the literature.[76,77] Electrodes were synthesized, characterized, and conductivity measured and confirmed before use. One common issue encountered in prototype fabrication is the design and optimization of components to work in concert. Potentiostat I/V data suggest an issue in regenerating the dye and proper electron flow. Currently, different prototypes are being fabricated to address conductivity, electrolyte, and dye performance, as well as the overall design of components. Figure 25 shows a proposed re-design of DSSC components.

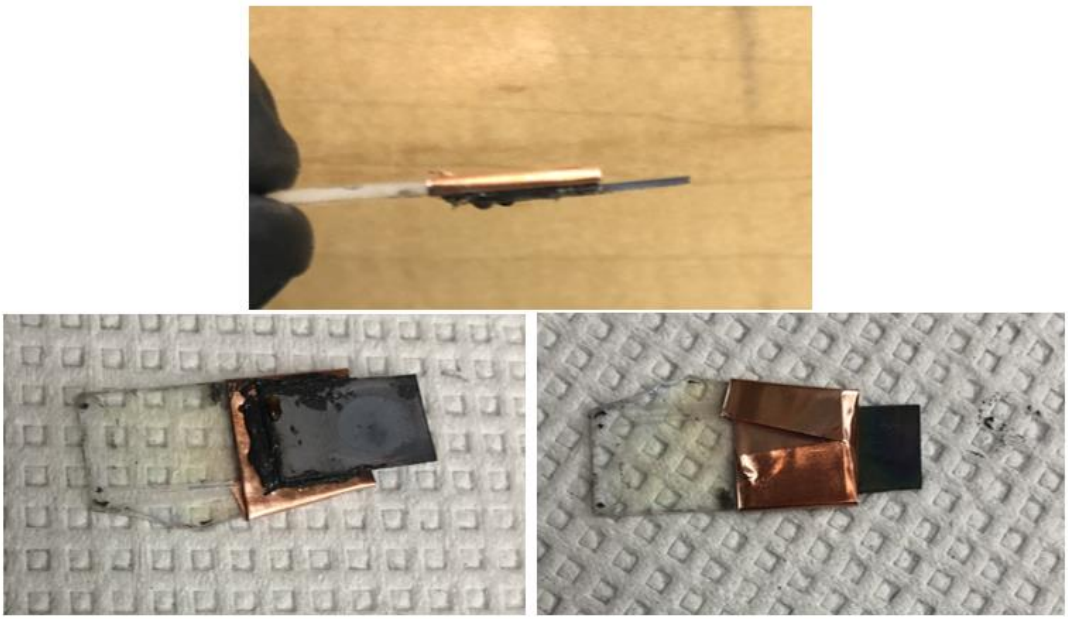

Figure 23. The completed dye-sensitized solar cell with undoped ZnO nanowires, N3 Dye, I^-/I_3^- electrolyte, and a copper electron facilitator.

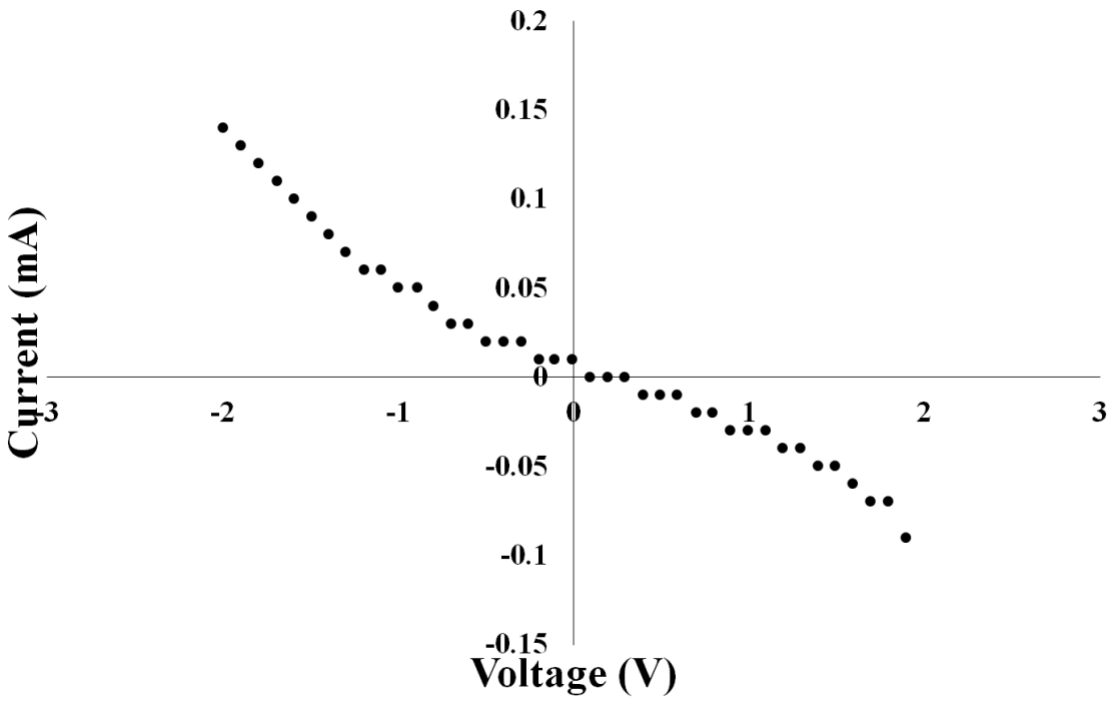

Figure 24. The IV curve of the fabricated undoped ZnO dye-sensitized solar cell.

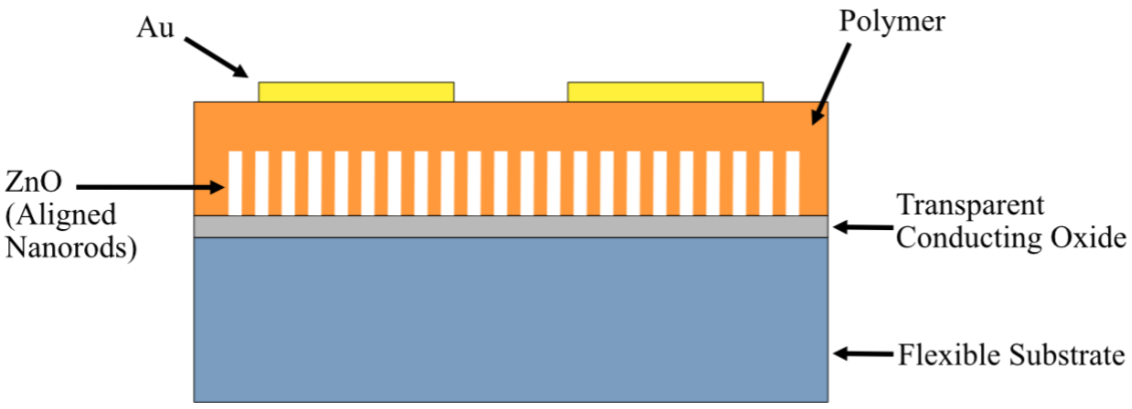

Figure 25. Proposed redesign of the dye-sensitized solar cell.

Conclusion

The fabrication of a dye-sensitized solar cell using undoped ZnO nanowires grown by a novel CVD method was conducted. Current/voltage data is typical of a diode rather than a photovoltaic cell. This could be thought of as the first step of a functioning photovoltaic cell as the semiconductor is forcing the electrons in one direction. Several issues encountered in the initial cell will be addressed in the next prototype. The method of applying the ITO layer is working as intended. The dye is adsorbing to the ZnO nanowires but could be improved to minimize the decomposition of the ZnO on the electrode. The electrolyte could be applied differently to ensure better encapsulation between the two electrodes. Alternatively, a solid-state electrolyte could be used to circumvent this issue by removing the need to encapsulate a liquid. This would also help with preventing a possible short in the cell itself by completely separating the two electrodes. The electron facilitator is also another component to examine. Copper is an impressive conductor; however, one shortcoming is forming oxides readily which reduces the conductivity of copper. With proper cleaning and removal of oxides and other films, then copper can be used as an electron facilitator in a short-lived DSSC.

REFERENCES

(1) Hashmi, G.; Miettunen, K.; Peltola, T.; Halme, J.; Asghar, I.; Aitola, K.; Toivola, M.; Lund, P. Review of Materials and Manufacturing Options for Large Area Flexible Dye Solar Cells. *Renew. Sustain. Energy Rev.* **2011**, *15* (8), 3717–3732.

(2) Kimitsuka, Y.; Hosono, E.; Ueno, S.; Zhou, H.; Fujihara, S. Fabrication of Porous Cubic Architecture of ZnO Using Zn-Terephthalate MOFs with Characteristic Microstructures. *Inorg. Chem.* **2013**, *52* (24), 14028–14033.

(3) Ashrafi, A.; Jagadish, C. Review of Zincblende ZnO: Stability of Metastable ZnO Phases. *J. Appl. Phys.* **2007**, *102* (7), 71101.

(4) Xu, L.; Li, X.; Zhan, Z.; Wang, L.; Feng, S.; Chai, X.; Lu, W.; Shen, J.; Weng, Z.; Sun, J. Catalyst-Free, Selective Growth of ZnO Nanowires on SiO2 by Chemical Vapor Deposition for Transfer-Free Fabrication of UV Photodetectors. *ACS Appl. Mater. Interfaces* **2015**, *7* (36), 20264–20271.

(5) Mo, Y.; Shi, F.; Qin, S.; Tang, P.; Feng, Y.; Zhao, Y.; Li, D. Facile Fabrication of Mesoporous Hierarchical Co-Doped ZnO for Highly Sensitive Ethanol Detection. *Ind. Eng. Chem. Res.* **2019**, *58* (19), 8061–8071.

(6) Han, S.; Zhang, H.; Lu, Y.; Xu, W.; Fang, M.; Liu, W.; Cao, P.; Zhu, D. Self-Powered Au/MgZnO/Nanolayered Ga-Doped ZnO/In Metal–Insulator–Semiconductor UV Detector with High Internal Gain at Deep UV Light under Low Voltage. *ACS Appl. Nano Mater.* **2020**, *3* (1), 120–130.

(7) Patel, M.; Kim, H.-S.; Kim, J.; Yun, J.-H.; Kim, S. J.; Choi, E. H.; Park, H.-H. Excitonic Metal Oxide Heterojunction (NiO/ZnO) Solar Cells for All-Transparent

Module Integration. *Sol. Energy Mater. Sol. Cells* **2017**, *170*, 246–253.

(8) Bekele, B.; Degefa, A.; Tesgera, F.; Jule, L. T.; Shanmugam, R.; Priyanka Dwarampudi, L.; Nagaprasad, N.; Ramasamy, K. Green versus Chemical Precipitation Methods of Preparing Zinc Oxide Nanoparticles and Investigation of Antimicrobial Properties. *J. Nanomater.* **2021**, *2021*, 9210817.

(9) Narath, S.; Koroth, S. K.; Shankar, S. S.; George, B.; Mutta, V.; Wacławek, S.; Černík, M.; Padil, V. V; Varma, R. S. Cinnamomum Tamala Leaf Extract Stabilized Zinc Oxide Nanoparticles: A Promising Photocatalyst for Methylene Blue Degradation. *Nanomaterials* . 2021.

(10) Hung, C. M.; Van Duy, L.; Thanh Le, D. T.; Nguyen, H.; Van Duy, N.; Hoa, N. D. ZnO Coral-like Nanoplates Decorated with Pd Nanoparticles for Enhanced VOC Gas Sensing. *J. Sci. Adv. Mater. Devices* **2021**, *6* (3), 453–461.

(11) Factori, I. M.; Amaral, J. M.; Camani, P. H.; Rosa, D. S.; Lima, B. A.; Brocchi, M.; da Silva, E. R.; Souza, J. S. ZnO Nanoparticle/Poly(Vinyl Alcohol) Nanocomposites via Microwave-Assisted Sol–Gel Synthesis for Structural Materials, UV Shielding, and Antimicrobial Activity. *ACS Appl. Nano Mater.* **2021**, *4* (7), 7371–7383.

(12) Dongare, S.; Singh, N.; Bhunia, H. Oxide-Derived Cu-Zn Nanoparticles Supported on N-Doped Graphene for Electrochemical Reduction of CO2 to Ethanol. *Appl. Surf. Sci.* **2021**, *556*, 149790.

(13) Alexiadou, M.; Kandyla, M.; Mousdis, G.; Kompitsas, M. Pulsed Laser Deposition of ZnO Thin Films Decorated with Au and Pd Nanoparticles with Enhanced

Acetone Sensing Performance. *Appl. Phys. A* **2017**, *123* (4), 262.

(14) Yao, Y.-F.; Tu, C.-G.; Chang, T.-W.; Chen, H.-T.; Weng, C.-M.; Su, C.-Y.; Hsieh, C.; Liao, C.-H.; Kiang, Y.-W.; Yang, C. C. Growth of Highly Conductive Ga-Doped ZnO Nanoneedles. *ACS Appl. Mater. Interfaces* **2015**, *7* (19), 10525–10533.

(15) Park, S.-H.; Park, J.-W.; Yang, S.-M.; Kim, K.-H.; Hwang, N.-M. Effect of Electric Bias on the Deposition Behavior of ZnO Nanostructures in the Chemical Vapor Deposition Process. *J. Phys. Chem. C* **2015**, *119* (44), 25047–25052.

(16) Ye, Z.; Wang, T.; Wu, S.; Ji, X.; Zhang, Q. Na-Doped ZnO Nanorods Fabricated by Chemical Vapor Deposition and Their Optoelectrical Properties. *J. Alloys Compd.* **2017**, *690*, 189–194.

(17) Bekermann, D.; Gasparotto, A.; Barreca, D.; Bovo, L.; Devi, A.; Fischer, R. A.; Lebedev, O. I.; Maccato, C.; Tondello, E.; Van Tendeloo, G. Highly Oriented ZnO Nanorod Arrays by a Novel Plasma Chemical Vapor Deposition Process. *Cryst. Growth Des.* **2010**, *10* (4), 2011–2018.

(18) Guan, Y. F.; Pedraza, A. J. Synthesis and Alignment of Zn and ZnO Nanoparticles by Laser-Assisted Chemical Vapor Deposition. *Nanotechnology* **2008**, *19* (4), 45609.

(19) Chapin, D. M.; Fuller, C. S.; Pearson, G. L. A New Silicon P-n Junction Photocell for Converting Solar Radiation into Electrical Power. *J. Appl. Phys.* **1954**, *25* (5), 676–677.

(20) Zhang, B.; Jie, J.; Zhang, X.; Ou, X.; Zhang, X. Large-Scale Fabrication of Silicon Nanowires for Solar Energy Applications. *ACS Appl. Mater. Interfaces* **2017**, *9* (40), 34527–34543.

(21) Kim, H.-S.; Lee, C.-R.; Im, J.-H.; Lee, K.-B.; Moehl, T.; Marchioro, A.; Moon, S.-J.; Humphry-Baker, R.; Yum, J.-H.; Moser, J. E.; Grätzel, M.; Park, N.-G. Lead Iodide Perovskite Sensitized All-Solid-State Submicron Thin Film Mesoscopic Solar Cell with Efficiency Exceeding 9%. *Sci. Rep.* **2012**, *2* (1), 591.

(22) Best Research-Cell Efficiency Chart https://www.nrel.gov/pv/cell-efficiency.html (accessed 2021 -11 -11).

(23) O'Regan, B.; Grätzel, M. A Low-Cost, High-Efficiency Solar Cell Based on Dye-Sensitized Colloidal TiO2 Films. *Nature* **1991**, *353* (6346), 737–740.

(24) Mor, G. K.; Kim, S.; Paulose, M.; Varghese, O. K.; Shankar, K.; Basham, J.; Grimes, C. A. Visible to Near-Infrared Light Harvesting in TiO2 Nanotube Array−P3HT Based Heterojunction Solar Cells. *Nano Lett.* **2009**, *9* (12), 4250–4257.

(25) Hossain, M. I.; Alharbi, F. H.; Tabet, N. Copper Oxide as Inorganic Hole Transport Material for Lead Halide Perovskite Based Solar Cells. *Sol. Energy* **2015**, *120*, 370–380.

(26) Haizhou, L.; Yuhang, L.; Paramvir, A.; Aditya, M.; R, T. W.; T, E. F.; Yingguo, Y.; Fan, F.; Zaiwei, W.; E, A. C.; I, C. B.; Anand, A.; Xin, Z.; Xiaoguo, L.; Yiqiang, Z.; M, Z. S.; Lyndon, E.; Ursula, R.; Lirong, Z.; Anders, H.; Michael, G. Vapor-Assisted Deposition of Highly Efficient, Stable Black-Phase FAPbI3

Perovskite Solar Cells. *Science (80-.).* **2020**, *370* (6512), eabb8985.

(27) Anta, J. A.; Guillén, E.; Tena-Zaera, R. ZnO-Based Dye-Sensitized Solar Cells. *J. Phys. Chem. C* **2012**, *116* (21), 11413–11425.

(28) Rühle, S.; Anderson, A. Y.; Barad, H.-N.; Kupfer, B.; Bouhadana, Y.; Rosh-Hodesh, E.; Zaban, A. All-Oxide Photovoltaics. *J. Phys. Chem. Lett.* **2012**, *3* (24), 3755–3764.

(29) Shockley, W.; Queisser, H. J. Detailed Balance Limit of Efficiency of P-n Junction Solar Cells. *J. Appl. Phys.* **1961**, *32* (3), 510–519.

(30) Zhao, F.; Deng, L.; Wang, K.; Han, C.; Liu, Z.; Yu, H.; Li, J.; Hu, B. Surface Modification of SnO2 via MAPbI3 Nanowires for a Highly Efficient Non-Fullerene Acceptor-Based Organic Solar Cell. *ACS Appl. Mater. Interfaces* **2020**, *12* (4), 5120–5127.

(31) Wang, H.; Yuan, J.; Xi, J.; Du, J.; Tian, J. Multiple-Function Surface Engineering of SnO2 Nanoparticles to Achieve Efficient Perovskite Solar Cells. *J. Phys. Chem. Lett.* **2021**, *12* (37), 9142–9148.

(32) Xie, Y.; Zhou, X.; Mi, H.; Ma, J.; Yang, J.; Cheng, J. High Efficiency ZnO-Based Dye-Sensitized Solar Cells with a 1H,1H,2H,2H-Perfluorodecyltriethoxysilane Chain Barrier for Cutting on Interfacial Recombination. *Appl. Surf. Sci.* **2018**, *434*, 1144–1152.

(33) Redmond, G.; Fitzmaurice, D.; Graetzel, M. Visible Light Sensitization by Cis-Bis(Thiocyanato)Bis(2,2’-Bipyridyl-4,4’-Dicarboxylato)Ruthenium(II) of a

Transparent Nanocrystalline ZnO Film Prepared by Sol-Gel Techniques. *Chem. Mater.* **1994**, *6* (5), 686–691.

(34) Mathew, S.; Yella, A.; Gao, P.; Humphry-Baker, R.; Curchod, B. F. E.; Ashari-Astani, N.; Tavernelli, I.; Rothlisberger, U.; Nazeeruddin, M. K.; Grätzel, M. Dye-Sensitized Solar Cells with 13% Efficiency Achieved through the Molecular Engineering of Porphyrin Sensitizers. *Nat. Chem.* **2014**, *6* (3), 242–247.

(35) Qin, Z.; Huang, Y.; Qi, J.; Liao, Q.; Wang, W.; Zhang, Y. Surface Destruction and Performance Reduction of the ZnO Nanowire Arrays Electrode in Dye Sensitization Process. *Mater. Lett.* **2011**, *65* (23), 3506–3508.

(36) Yan, F.; Huang, L.; Zheng, J.; Huang, J.; Lin, Z.; Huang, F.; Wei, M. Effect of Surface Etching on the Efficiency of ZnO-Based Dye-Sensitized Solar Cells. *Langmuir* **2010**, *26* (10), 7153–7156.

(37) Wei, H.; Luo, J.-W.; Li, S.-S.; Wang, L.-W. Revealing the Origin of Fast Electron Transfer in TiO2-Based Dye-Sensitized Solar Cells. *J. Am. Chem. Soc.* **2016**, *138* (26), 8165–8174.

(38) Van de Walle, C. G. Hydrogen as a Cause of Doping in Zinc Oxide. *Phys. Rev. Lett.* **2000**, *85* (5), 1012–1015.

(39) Liu, L.; Hong, K.; Ge, X.; Liu, D.; Xu, M. Controllable and Rapid Synthesis of Long ZnO Nanowire Arrays for Dye-Sensitized Solar Cells. *J. Phys. Chem. C* **2014**, *118* (29), 15551–15555.

(40) Rusdi, R.; Rahman, A. A.; Mohamed, N. S.; Kamarudin, N.; Kamarulzaman, N.

Preparation and Band Gap Energies of ZnO Nanotubes, Nanorods and Spherical Nanostructures. *Powder Technol.* **2011**, *210* (1), 18–22.

(41) Báez-Rodríguez, A.; Zamora-Peredo, L.; Soriano-Rosales, M. G.; Hernández-Torres, J.; García-González, L.; Calderón-Olvera, R. M.; García-Hipólito, M.; Guzmán-Mendoza, J.; Falcony, C. ZnO Nanocolumns Synthesized by Chemical Bath Process and Spray Pyrolysis: Ultrasonic and Mechanical Dispersion of ZnO Seeds and Their Effect on Optical and Morphological Properties. *J. Lumin.* **2020**, *218*, 116830.

(42) Liu, K. W.; Chen, R.; Xing, G. Z.; Wu, T.; Sun, H. D. Photoluminescence Characteristics of High Quality ZnO Nanowires and Its Enhancement by Polymer Covering. *Appl. Phys. Lett.* **2010**, *96* (2), 023111.

(43) Vempati, S.; Mitra, J.; Dawson, P. One-Step Synthesis of ZnO Nanosheets: A Blue-White Fluorophore. *Nanoscale Res. Lett.* **2012**, *7* (1), 470.

(44) Li, L.; Shan, C. X.; Li, B. H.; Yao, B.; Zhang, J. Y.; Zhao, D. X.; Zhang, Z. Z.; Shen, D. Z.; Fan, X. W.; Lu, Y. M. The Compensation Source in Nitrogen Doped ZnO. *J. Phys. D. Appl. Phys.* **2008**, *41* (24), 245402.

(45) Xiu, F. X.; Yang, Z.; Mandalapu, L. J.; Liu, J. L. Donor and Acceptor Competitions in Phosphorus-Doped ZnO. *Appl. Phys. Lett.* **2006**, *88* (15), 152116.

(46) Lee, W.; Jeong, M.-C.; Myoung, J.-M. Optical Characteristics of Arsenic-Doped ZnO Nanowires. *Appl. Phys. Lett.* **2004**, *85* (25), 6167–6169.

(47) Liang, H.; Chen, Y.; Xia, X.; Feng, Q.; Liu, Y.; Shen, R.; Luo, Y.; Du, G.

Influence of Sb Valency on the Conductivity Type of Sb-Doped ZnO. *Thin Solid Films* **2015**, *589*, 199–202.

(48) Jun, W.; Yintang, Y. Deposition of K-Doped p Type ZnO Thin Films on (0001) Al2O3 Substrates. *Mater. Lett.* **2008**, *62* (12), 1899–1901.

(49) Xiang, B.; Wang, P.; Zhang, X.; Dayeh, S. A.; Aplin, D. P. R.; Soci, C.; Yu, D.; Wang, D. Rational Synthesis of P-Type Zinc Oxide Nanowire Arrays Using Simple Chemical Vapor Deposition. *Nano Lett.* **2007**, *7* (2), 323–328.

(50) Yang, W. S.; Noh, J. H.; Jeon, N. J.; Kim, Y. C.; Ryu, S.; Seo, J.; Seok, S. Il. High-Performance Photovoltaic Perovskite Layers Fabricated through Intramolecular Exchange. *Science (80-.).* **2015**, *348* (6240), 1234 LP – 1237.

(51) Baek, S.-D.; Biswas, P.; Kim, J.-W.; Kim, Y. C.; Lee, T. Il; Myoung, J.-M. Low-Temperature Facile Synthesis of Sb-Doped p-Type ZnO Nanodisks and Its Application in Homojunction Light-Emitting Diode. *ACS Appl. Mater. Interfaces* **2016**, *8* (20), 13018–13026.

(52) Yao, Z.; Tang, K.; Xu, Y.; Du, Q.; Li, J.; Hao, L.; Shen, Y.; Zhu, S.; Gu, S. Synthesis, Characterization and UV Photodetector Application of Sb-Doped ZnO Nanowires. *J. Lumin.* **2020**, *221*, 117025.

(53) Luo, C.; Ho, L.-P.; Azad, F.; Anwand, W.; Butterling, M.; Wagner, A.; Kuznetsov, A.; Zhu, H.; Su, S.; Ling, F. C.-C. Sb-Related Defects in Sb-Doped ZnO Thin Film Grown by Pulsed Laser Deposition. *J. Appl. Phys.* **2017**, *123* (16), 161525.

(54) Nasser, R.; Elhouichet, H. Production of Acceptor Complexes in Sol-Gel ZnO

Thin Films by Sb Doping. *J. Lumin.* **2018**, *196*, 11–19.

(55) Alsmadi, A. M.; Salameh, B.; Kerr, L. L.; Eid, K. F. Influence of Antimony Doping on the Electronic, Optical and Luminescent Properties of ZnO Microrods. *Phys. B Condens. Matter* **2018**, *545*, 519–526.

(56) Wang, C.-C.; Lin, W.-C.; Shieu, F.-S.; Shih, H. C. Enhanced Optoelectronic Properties of Thermally Evaporated Sb-Doped ZnO Nanowires via Defect Structures. *AIP Adv.* **2019**, *9* (12), 125019/1-125019/8.

(57) Bauer, C.; Boschloo, G.; Mukhtar, E.; Hagfeldt, A. Electron Injection and Recombination in Ru(Dcbpy)2(NCS)2 Sensitized Nanostructured ZnO. *J. Phys. Chem. B* **2001**, *105* (24), 5585–5588.

(58) Odobel, F.; Pellegrin, Y. Recent Advances in the Sensitization of Wide-Band-Gap Nanostructured p-Type Semiconductors. Photovoltaic and Photocatalytic Applications. *J. Phys. Chem. Lett.* **2013**, *4* (15), 2551–2564.

(59) Suja, M.; Bashar, S. B.; Morshed, M. M.; Liu, J. Realization of Cu-Doped p-Type ZnO Thin Films by Molecular Beam Epitaxy. *ACS Appl. Mater. Interfaces* **2015**, *7* (16), 8894–8899.

(60) Brahma, S.; Yeh, Y.-W.; Huang, J.-L.; Liu, C.-P. Cu-Doped p-Type ZnO Nanostructures as Unique Acetone Sensor at Room Temperature (~25 °C). *Appl. Surf. Sci.* **2021**, *564*, 150351.

(61) Liau, L. C.-K.; Huang, J.-S. Energy-Level Variations of Cu-Doped ZnO Fabricated through Sol-Gel Processing. *J. Alloys Compd.* **2017**, *702*, 153–160.

(62) Ghahramanifard, F.; Rouhollahi, A.; Fazlolahzadeh, O. Electrodeposition of Cu-Doped p-Type ZnO Nanorods; Effect of Cu Doping on Structural, Optical and Photoelectrocatalytic Property of ZnO Nanostructure. *Superlattices Microstruct.* **2018**, *114*, 1–14.

(63) Ge, Z.; Wang, C.; Chen, T.; Chen, Z.; Wang, T.; Guo, L.; Qi, G.; Liu, J. Preparation of Cu-Doped ZnO Nanoparticles via Layered Double Hydroxide and Application for Dye-Sensitized Solar Cells. *J. Phys. Chem. Solids* **2021**, *150*, 109833.

(64) Zhuang, S.; Lu, M.; Zhou, N.; Zhou, L.; Lin, D.; Peng, Z.; Wu, Q. Cu Modified ZnO Nanoflowers as Photoanode Material for Highly Efficient Dye Sensitized Solar Cells. *Electrochim. Acta* **2019**, *294*, 28–37.

(65) Rojas-Michea, C.; Morel, M.; Gracia, F.; Morell, G.; Mosquera, E. Influence of Copper Doping on Structural, Morphological, Optical, and Vibrational Properties of ZnO Nanoparticles Synthesized by Sol Gel Method. *Surfaces and Interfaces* **2020**, *21*, 100700.

(66) Saha, R. K.; Debanath, M. K.; Saikia, E. Multifractal Analysis of ZnO Nanoparticles. *Mater. Sci. Eng. C* **2020**, *106*, 110177.

(67) Ahn, C. H.; Kim, Y. Y.; Kim, D. C.; Mohanta, S. K.; Cho, H. K. A Comparative Analysis of Deep Level Emission in ZnO Layers Deposited by Various Methods. *J. Appl. Phys.* **2009**, *105* (1), 013502.

(68) Bylander, E. G. Surface Effects on the Low-energy Cathodoluminescence of Zinc Oxide. *J. Appl. Phys.* **1978**, *49* (3), 1188–1195.

(69) El Sayed, A. M.; Said, G.; Taha, S.; Ibrahim, A.; Yakuphanoglu, F. Influence of Copper Incorporation on the Structural and Optical Properties of ZnO Nanostructured Thin Films. *Superlattices Microstruct.* **2013**, *62*, 47–58.

(70) Yuhas, B. D.; Yang, P. Nanowire-Based All-Oxide Solar Cells. *J. Am. Chem. Soc.* **2009**, *131* (10), 3756–3761.

(71) Guo, Z.; Jena, A. K.; Takei, I.; Kim, G. M.; Kamarudin, M. A.; Sanehira, Y.; Ishii, A.; Numata, Y.; Hayase, S.; Miyasaka, T. VOC Over 1.4 V for Amorphous Tin-Oxide-Based Dopant-Free CsPbI2Br Perovskite Solar Cells. *J. Am. Chem. Soc.* **2020**, *142* (21), 9725–9734.

(72) Ahmed, A. S. A.; Xiang, W.; Abdelmotalleib, M.; Zhao, X. Efficient NiO Impregnated Walnut Shell-Derived Carbon for Dye-Sensitized Solar Cells. *ACS Appl. Electron. Mater.* **2022**.

(73) Janotti, A.; Van de Walle, C. G. Native Point Defects in ZnO. *Phys. Rev. B* **2007**, *76* (16), 165202.

(74) Erten-Ela, S.; Ocakoglu, K.; Tarnowska, A.; Vakuliuk, O.; Gryko, D. T. Performance of Zinc Chlorophyll Based Molecules for Dye Sensitized Solar Cell. *Dye. Pigment.* **2015**, *114*, 129–137.

(75) Richhariya, G.; Kumar, A.; Tekasakul, P.; Gupta, B. Natural Dyes for Dye Sensitized Solar Cell: A Review. *Renew. Sustain. Energy Rev.* **2017**, *69*, 705–718.

(76) Ling, T.; Song, J.-G.; Chen, X.-Y.; Yang, J.; Qiao, S.-Z.; Du, X.-W. Comparison of ZnO and TiO2 Nanowires for Photoanode of Dye-Sensitized Solar Cells. *J.*

Alloys Compd. **2013**, *546*, 307–313.

(77) Boschloo, G.; Hagfeldt, A. Characteristics of the Iodide/Triiodide Redox Mediator in Dye-Sensitized Solar Cells. *Acc. Chem. Res.* **2009**, *42* (11), 1819–1826.

VITA

PROFESSIONAL EXPERIENCE

Research Assistant

Sam Houston State University Chemistry Department

- Synthesized ZnO nanoparticles via chemical vapor deposition
- Characterized samples using XRD, SEM-EDS, and photoluminescence
- Fabricated dye-sensitized solar cells
- Trained incoming assistants on experimental procedures and proper instrumentation techniques

Teaching Assistant

Sam Houston State University Chemistry Department

- Taught chemistry labs in the fields of physical chemistry and quantitative analysis
- Trained students on how to properly use GC-FID, AAS, UV-Vis, Gaussian, and Excel
- Carried out related responsibilities such as grading and tutoring

HONORS

- Dean's List: Fall 2018 and Spring 2019
- Robert Welch Foundation Research Fellowship: Summers of 2018, 2019, and 2021

PUBLICATIONS

- Trad, T., Blount, P., Romero, Z., Thompson, D. Zinc Oxide Nanostructure Synthesis on Si(100) by Vapor Phase Transport and the Effect of Antimony Doping

on Photoelectric Properties, Morphology, and Structure *MRS Advances* **2020**, *5*, 1687–1695. https://doi.org/10.1557/adv.2020.150

- Stephen, H., Blount, P., Trad, T. Chapter 8 - Catalytic and noncatalytic growth of ZnO nanostructures on different substrates, and Sb-doped ZnO nanostructures on Au-catalyzed Si(100): Components for potential utilization in three-dimensional dye-sensitized solar cells. In K. Y. Cheong & A. Apblett (Eds.), *Sustainable Materials and Green Processing for Energy Conversion* **2020**, pp 263–277. https://doi.org/https://doi.org/10.1016/B978-0-12-822838-8.00013-2

PRESENTATIONS

- Blount, P.; Romero, Z.; Trad, T.; Balaraman, R. "P-type antimony-doped ZnO nanostructures: Vapor phase transport synthesis and room temperature photoluminescence" Oral presentation, ACS Southwest Regional and Rocky Mountain Regional Meeting, El Paso, TX, November 13-16, 2020.
- Blount, P.; Trad, T.; Stephen, H.; Balaraman, R. "Comparison of Sb(III) and Sb(V) as donors for p-type Sb-doped ZnO nanostructures: Vapor phase transport synthesis, and room temperature photoluminescence" Oral presentation, 261st ACS National Meeting, Remote, April 5-16, 2021.
- Blount, P.; Marder, L.; Trad, T. "The synthesis of Cu-doped ZnO Nanowires via a Novel CVD Method for Utilization in Grätzel-type dye-sensitized solar cells" Oral presentation, ACS Southwest Regional Meeting of the American Chemical Society, Austin, TX, October 31 - November 3, 2021

- Blount, P.; Tarek, T.; “Antimony and copper-doping in ZnO nanorods via vapor phase transport and incorporation: Morphological and photoelectronic effects” Oral presentation, 262nd ACS National Meeting, San Diego, CA, March 20-24, 2022